- Article type: paper (6650 words, excluding abstract and References list)
- Date text written: 14.10.2018; Date text modified: 02/03/2019
- Number of figures: 16 in main text; 5 in appendices

A case study of liquefaction: demonstrating the application of an advanced model and understanding the pitfalls of the simplified procedure

Author 1 (corresponding author)

- Vasiliki (Vasia) Tsaparli, PhD MSc MEng DIC AFHEA
- Ørsted, London UK, formerly Imperial College London
- vasts@orsted.co.uk; v.tsaparli@gmail.com
- ORCID number: 0000-0002-5646-0650

Author 2

- Stavroula Kontoe, PhD MSc MEng DIC
- Department of Civil & Environmental Engineering, Imperial College London, London, UK
- stavroula.kontoe@imperial.ac.uk
- ORCID number: 0000-0002-8354-8762

Author 3

- David M G Taborda, PhD MSC DIC
- Department of Civil & Environmental Engineering, Imperial College London, London, UK
- d.taborda@imperial.ac.uk
- ORCID number: 0000-0001-5391-2087

Author 4

- David M Potts, BSc PhD DSc FREng FICE FCGI, GCG Professor of Geotechnical Engineering
- Department of Civil & Environmental Engineering, Imperial College London, London, UK
- d.potts@imperial.ac.uk
- ORCID number:0000-0001-9547-8469

Abstract

The complexity of advanced constitutive models often dictates that their capabilities are only demonstrated in the context of model testing under controlled conditions. In the case of earthquake engineering and liquefaction in particular, this restriction is magnified by the difficulties in measuring field behaviour under seismic loading. In this paper, the well documented case of the Canterbury Earthquake Sequence in New Zealand, for which extensive field and laboratory data are available, is utilised to demonstrate the accuracy of a bounding surface plasticity model in fully-coupled finite element analyses. A strong motion station with manifestation of liquefaction and the second highest peak vertical ground acceleration during the M_w 6.2 February 2011 event is modelled. An empirical assessment predicted no liquefaction for this station, making this an interesting case for rigorous numerical modelling. The calibration of the model aims at capturing both the laboratory tests and the field measurements in a consistent manner. The characterisation of the ground conditions is presented, while, to specify the bedrock motion, the records of two stations without liquefaction are deconvolved and scaled to account for wave attenuation with distance. The numerical predictions are compared to both the horizontal and vertical acceleration records and other field observations, showing a remarkable agreement, also demonstrating that the high vertical accelerations can be attributed to compressional resonance. The results provide further insights into the underperformance of the simplified procedure.

Keywords

liquefaction; dynamics; field instrumentation; numerical modelling; bounding surface plasticity model; validation; simplified procedure; horizontal and vertical records

List of notation

A	Plastic hardening modulus (BSPM)
A_d	Dilatancy coefficient (BSPM)
A_0	Dilatancy constant – maximum value of the dilatancy coefficient (BSPM)

$A_{0,min}$	Minimum value of the dilatancy coefficient (BSPM)
A_2	Plastic hardening modulus corresponding to the secondary yield surface (BSPM)
a	Acceleration
a_x	Acceleration in the horizontal direction
a_y	Acceleration in the vertical direction
$a_{0,c}$, $a_{1,c}$, $a_{2,c}$, $b_{0,c}$	Parameters controlling the shear stiffness degradation (ICG3S)
a_1	Defines the ratio of the minimum over the maximum elastic tangent shear modulus, G_{min}/G_{max} (BSPM)
B	Small strain stiffness shear modulus constant (BSPM)
B_{CRR}	Slope of a power law fit to the cyclic resistance ratio (CRR) curve
b	Parameters controlling the non-linearity of the A_d expression (BSPM)
b_d	Parameter defining the value of b at $p'_0 = 0$ kPa (BSPM)
b_{max}	Parameter defining upper boundary of b (BSPM)
C_f	Parameter controlling compliance on load reversal following a dilative stress path (BSPM)
C_u	Coefficient of uniformity
D	Damping ratio; dilatancy ratio (BSPM)
D_r	Relative density
D_{10}	Effective size (10% of the particles are smaller than this size)
D_{50}	50% of the particles are smaller than this size
$d^{c,b,d}$	Distance to the CS/bounding/dilatancy surface (BSPM)
$d^{d,SR}$	Distance to the dilatancy surface from the last stress reversal in the deviatoric plane (BSPM)
d^b_{ref}	Opening of the bounding surface in the deviatoric plane (BSPM)

d_1, d_2, d_3	Parameters controlling the position and non-linearity of the b expression in A_d (BSPM)
$d'_{1,G}$, $d''_{1,G}$, $d_{2,G}$, $d_{3,G}$, $d_{4,G}$	Parameters defining the variation of the scaling factor in ICG3S
e	Void ratio
e_{CS}	Void ratio at Critical State
$(e_{CS})_{ref}$	Critical State void ratio at a reference pressure p'_{ref}
e_{max}	Void ratio limit on the determination of the plastic modulus (BSPM); maximum void ratio
e_{min}	Minimum void ratio
e_0	Void ratio after consolidation
F_1	Primary yield surface (BSPM)
F_2	Secondary yield surface (BSPM)
f	Frequency
f	Deviatoric component of the fabric tensor
$f_G(e)$	Function defining the dependence of G_{max} on the void ratio (ICG3S)
f_p	Spherical component of the fabric tensor
f_1	Fundamental or natural frequency
G_{max}	Maximum or small strain shear modulus
G_{max}^{SR}	Maximum shear modulus at last stress reversal (BSPM)
G_{min}	Minimum degraded elastic tangent shear modulus (BSPM; ICG3S)
G_{sec}	Secant shear modulus
G_{tan}	Tangent shear modulus
G_0	Basic maximum shear modulus in G_{max} equation (ICG3S)
g	Gravitational acceleration

$g(\theta,c)$	Interpolation function (BSPM)
H	Fabric index (BSPM)
H_0	Fabric index constant (BSPM)
H_1	Thickness of surficial "crust" layer
H_2	Thickness of liquefied sand layer
h_b	Component of the hardening modulus related to d^b and p' (BSPM)
h_e	Component of the hardening modulus related to the void ratio (BSPM)
h_g	Component of the hardening modulus related to G_{tan} (BSPM)
h_f	Fabric scalar – component of the hardening modulus (BSPM)
h_0	Plastic modulus constant (BSPM)
I_c	Soil behaviour type index
$\mathbf{I_3}$	Second order identity tensor
K_{tan}	Tangent bulk modulus
K_σ	Overburden correction factor
K_0	Coefficient of earth pressure at rest
k	Permeability
k_c^b	Parameter defining the size of the bounding surface
k_c^d	Parameter defining the size of the dilatancy surface
k_{max}	Maximum permeability at the time of liquefaction
k_0	Initial static permeability as measured in conventional laboratory testing
M_c^c	Stress ratio (q/p') defining the critical state shear strength in triaxial compression
M_e^c	Stress ratio (q/p') defining the critical state shear strength in q-p' space in triaxial extension

M_w	Moment magnitude
m	Radius of the yield surface (BSPM)
m_G	Parameter defining the non-linearity of the dependency of G_{max} on p' (ICG3S)
N	Number of loading cycles to liquefaction
N_T	Scaling factor in the expression for the elastic tangent shear modulus introducing Masing behaviour (BSPM)
n	Porosity
$\mathbf{n}$	Unit stress ratio tensor defining the loading direction (BSPM)
n_k	Controls the effect of r_u on the permeability
P_1	Primary plastic potential (BSPM)
P_2	Secondary plastic potential (BSPM)
p	Pore water pressure
p'	Mean effective stress – first invariant of the stress tensor
p'_{ref}	Reference pressure (i.e. at atmospheric pressure) (BSPM, ICG3S)
p'^{SR}	Mean effective stress at last stress reversal (BSPM)
p'_{YS}	Determines the location of the secondary yield surface (BSPM)
p'_0	Mean effective stress level after consolidation
$p'_{0,A}$	Parameter in b expression for the dilatancy coefficient (BSPM)
q	Triaxial deviatoric stress
q_{amp}	Deviatoric stress amplitude
q_{c1N}	Normalised dimensionless cone penetration resistance
$R_{G,min}$	Parameter defining G_{min} (ICG3S)

$\mathbf{r}$	Deviatoric stress ratio tensor (BSPM)
$\mathbf{r}^{\mathbf{SR}}$	Deviatoric stress ratio tensor at the last stress reversal (BSPM)
$\bar{\mathbf{r}}$	Radial deviatoric stress ratio tensor (BSPM)
$\mathrm{r_u}$	Excess pore water pressure ratio
$\mathrm{r_{u,max}}$	Maximum excess pore water pressure ratio
$\mathrm{r_{u,final}}$	r_u at the end of the dynamic analysis
r_u^*	Cut-off excess pore pressure ratio value at which the permeability attains its maximum value, $\mathrm{k_{max}}$
$\mathbf{s}$	Deviatoric stress tensor (BSPM)
t	Time
u	Solid phase displacement
$\mathrm{V_s}$	S-wave velocity
$\mathrm{V_{s1}}$	Overburden-corrected shear wave velocity
W	East-West direction
$\boldsymbol{\alpha}$	Back-stress ratio tensor defining the axis of the primary yield surface (BSPM)
$\boldsymbol{\alpha}^{\mathrm{c,b,d}}$	Image back-stress ratio tensor on the CS/bounding/dilatancy surface (BSPM)
α_{G}	Determines the effect of the elastic tangent shear modulus on the plastic modulus (BSPM)
β	Determines the effect of the distance to the bounding surface on the plastic modulus (BSPM)
γ	Determines the effect of void ratio on the plastic modulus (BSPM)
γ_b	Bulk unit weight
γ_c	Shear strain amplitude

γ_1	Cut-off strain for the degradation of the elastic tangent shear modulus (BSPM)
Δ	Change
Δu	Change in pore water pressure
ε_{α}	Axial strain
ε_{vol}	Volumetric strain
ε_{vol}^{p}	Plastic volumetric strain
ζ	Determines the effect of principal stress on the fabric index (BSPM)
θ	Lode's angle – third invariant of the stress tensor
κ	Parameter controlling the nonlinearity of the degradation of the elastic tangent shear modulus (BSPM)
Λ	Scalar multiplier in the flow rule (BSPM)
λ	Slope of Critical State Line in $e - \ln p'$ space (BSPM)
μ	Determines the effect of p' on the plastic modulus (BSPM)
ν	Poisson's ratio
ξ	Exponent for power law for Critical State Line (BSPM)
ρ_{∞}	Spectral radius at infnity
σ'	Effective stress
$\sigma'_{1,0}$	Principal effective stress after consolidation
φ'_{CS}	Angle of shearing resistance at Critical State
χ_{ref}^{r}	Distance of the current stress state from the last shear reversal point in the deviatoric plane (BSPM)
ψ	State parameter
ψ_0	State parameter after consolidation

Abbreviations and acronyms

B10	Bradley (2010) GMPE
BC16	Bozorgnia & Campbell (2016) GMPE
BE	Bender element
BSPM	Bounding surface plasticity model
CBD	Central Business District
CB03	Campbell & Bozorgnia (2003) GMPE
CES	Canterbury earthquake sequence
CID	Isotropically consolidated drained
CIU	Isotropically consolidated undrained
CPT	Cone penetration test
CPTu	Piezo cone penetration test
CRR	Cyclic resistance ratio
CSL	Critical State Line
CSR	Cyclic stress ratio
DH	Downhole test
EERA	Computer program for equivalent-linear analysis (Bardet *et al.*, 2000)
FA	Fourier amplitude
FBM	Fitzgerald Bridge site in Christchurch
FC	Fines content
FE	Finite element
FS	Fourier spectrum
GMPE	Ground motion prediction equation
GP	Gel-Push
GWT	Ground Water Table

ICFEP	Imperial College Finite Element Program
ICG3S	Imperial College Generalised Small Strain Stiffness model
K1	Kilmore site in Christchurch
LPCC	Lyttelton Port Company Station
LS_k10^{-3}	FE analysis with input ground motion the deconvolved and scaled LPCC horizontal component and a constant sand permeability of 10^{-3} m/s (10 times higher than the static value)
LS_V_k	FE analysis with input ground motion the deconvolved and scaled LPCC horizontal component and a variable sand permeability
LS1, LS2, LS3, LS4	Reference FE analyses with input ground motion the deconvolved and scaled LPCC horizontal component (static sand permeability k=10^{-4} m/s)
LV1, LV2, LV3, LV4	Reference FE analyses with input ground motion the deconvolved and scaled LPCC vertical component (static sand permeability k=10^{-4} m/s)
LV1_GR	FE analysis with input ground motion the deconvolved and scaled LPCC vertical component, including the Riccarton gravel horizon down to bedrock in the modelled stratigraphy (static sand permeability k=10^{-4} m/s)
MASW	Multi-channel Analysis of Surface Waves
M-CPT	McGann *et al.* (2014a,b) CPT-V_s correlation (Christchurch-specific)
MT	Moist-tamped
NZGD	New Zealand Geotechnical Database
OCR	Overconsolidation ratio
PGA	Peak ground acceleration
PI	Plasticity index

PRPC	Pages Road Pumping Station
P-wave	Compressional wave
RHSC	Riccarton High School station
RN1, RN2, RN3, RN4	Reference FE analyses with input ground motion the deconvolved and scaled RHSC horizontal component (static sand permeability $k=10^{-4}$ m/s)
RV1, RV2, RV3, RV4	Reference FE analyses with input ground motion the deconvolved and scaled RHSC vertical component (static sand permeability $k=10^{-4}$ m/s)
SD	Standard deviation
SMS	Strong motion station
SPT	Standard Penetration Test
SR	Shear reversal
S-wave	Shear wave
UP	Vertical component
V_k	Variable permeability

1 Introduction

In the field of earthquake geotechnics, and liquefaction in particular, the use of advanced constitutive models to replicate field response is uncommon due to a lack of i) field monitoring and ii) extensive material characterisation, which are required for an adequate model calibration. Therefore, physical modelling, such as centrifuge testing, is often used as a benchmark for numerical analyses (Arulanandan & Scott, 1993; Andrianopoulos *et al.*, 2010; Taborda, 2011). The 2010-2011 Canterbury Earthquake Sequence (CES) in New Zealand offers a unique opportunity for exploring the application of advanced numerical analysis to the prediction of ground motion during extreme seismic events, as it was recorded by a dense network of strong motion stations at various distances from the earthquake epicentre, while data from an extensive field and laboratory programme has also become available.

Prior to the 2010-2011 CES, limited attention had been given to modelling liquefaction in Christchurch, with the majority of site response analyses considering only soil non-linearity due to strain development (Elder *et al.*, 1991; Berrill *et al.*, 1993). More recent examples of such analyses are Garini *et al.* (2013), Arefi (2014) and Markham *et al.* (2016). Studies that accounted for residual excess pore pressures used either simplified constitutive models coupled with empirical excess pore pressure generation expressions (Smyrou *et al.*, 2011; Markham *et al.*, 2016) or advanced constitutive models which, however, were not calibrated based on site-specific laboratory data, as these were not available at the time (Garini *et al.*, 2013). Markham *et al.* (2016) also carried out site response analyses with the use of an advanced bounding surface plasticity model, although no information on its calibration was given. Additionally, despite the surprisingly large vertical accelerations registered during the CES, no site-specific vertical motion site response analyses were found to have been carried out.

Therefore, in this paper, the performance of a bounding surface plasticity model (BSPM), calibrated based on site-specific laboratory data, is evaluated by reproducing the response of a strong motion station (SMS) in Christchurch, as registered during the M_w 6.2 22nd February 2011 Christchurch event, the most damaging earthquake of the various events comprising the sequence. A simpler cyclic non-linear model is also used to model non-liquefiable strata. The chosen station is a "false negative" case, i.e. it exhibited liquefaction characteristics and surface manifestation, despite the fact that an empirical assessment predicted no liquefaction (Wotherspoon *et al.*, 2015). It also registered unexpectedly high vertical accelerations, making this a very interesting case for further investigation. Fully-coupled effective stress-based finite element (FE) analyses using the Imperial College Finite Element Program (ICFEP, Potts & Zdravković, 1999) and modelling both the horizontal and vertical components are subsequently carried out and the numerical results are compared to the recorded ground surface acceleration time-histories, as well as to field observations of liquefaction and predictions of empirical assessments.

The contribution of the present study is threefold: firstly, it highlights the challenges faced when modelling field case studies with advanced constitutive models, but also presents a method to ensure consistency between element testing and field data, validating the use of a BSPM in predicting field response. Secondly, the numerical predictions offer a means of exploring the reasons behind the underperformance of the simplified liquefaction procedure. Thirdly, it further validates the concept of resonance in the vertical direction as a mechanism of generation of high vertical ground surface accelerations (Tsaparli *et al.*, 2016; 2017a; 2018) against field data.

2 Selection of site and subsurface characterisation

The composition of the Canterbury Plains consists of the Springston Formation of alluvial origin (gravel, silt and peat swamp deposits) and the Christchurch Formation comprising predominantly marine sand (Brown *et al.*, 1995). These are underlain by the Riccarton gravel, which, together with older layers of gravel, can reach depths down to 500 m (Brown *et al.*, 1995). Christchurch sands can be characterised by various non-plastic fines contents (FC) (up to 80%), which can alter greatly their Critical State Line (CSL), small-strain stiffness and cyclic strength (Rees, 2010; Arefi, 2014; Taylor, 2015). Therefore, the selection of a site to undertake site response analyses was based on the following criteria:

1. a relatively uniform sand profile down to the Riccarton Gravel, to simplify the complex soil stratigraphy;

2. being far away from any free face to exclude the possibility of lateral spreading;

3. reported liquefaction ejecta and post-liquefaction settlements with evident liquefaction characteristics in the horizontal acceleration record;

4. high ground water table (GWT) and high vertical acceleration amplitudes to examine the case of resonance in compression, as presented in Tsaparli *et al.* (2016; 2017a; 2018).

The Pages Road Pumping station (PRPC), east of the Central Business District (CBD), was chosen for the analyses as it met all criteria. The horizontal component oriented roughly along East-West was modelled, being the direction that recorded the highest peak ground acceleration (PGA) at almost all stations during the February event (Tasiopoulou *et al.*, 2011). At station PRPC the PGA in this direction was 0.664*g*. The vertical motion, given the high ground water table (GWT) and consequent absence of nonlinearity as in this case the response in the vertical direction is controlled by the high compressibility of the water, was characterised by high frequency and a PGA of 1.63*g*, the second highest during the February event.

The stratigraphy at the site of interest, inferred from nearby cone penetration tests (CPTs) and boreholes available through the New Zealand Geotechnical Database, NZGD, (NZGD, 2016), is summarised in Figure 1a. Two out of the four nearby CPTs examined met refusal at 28 m depth, due to the presence of the top of the Riccarton Gravel at that depth (Wotherspoon *et al.*, 2015).

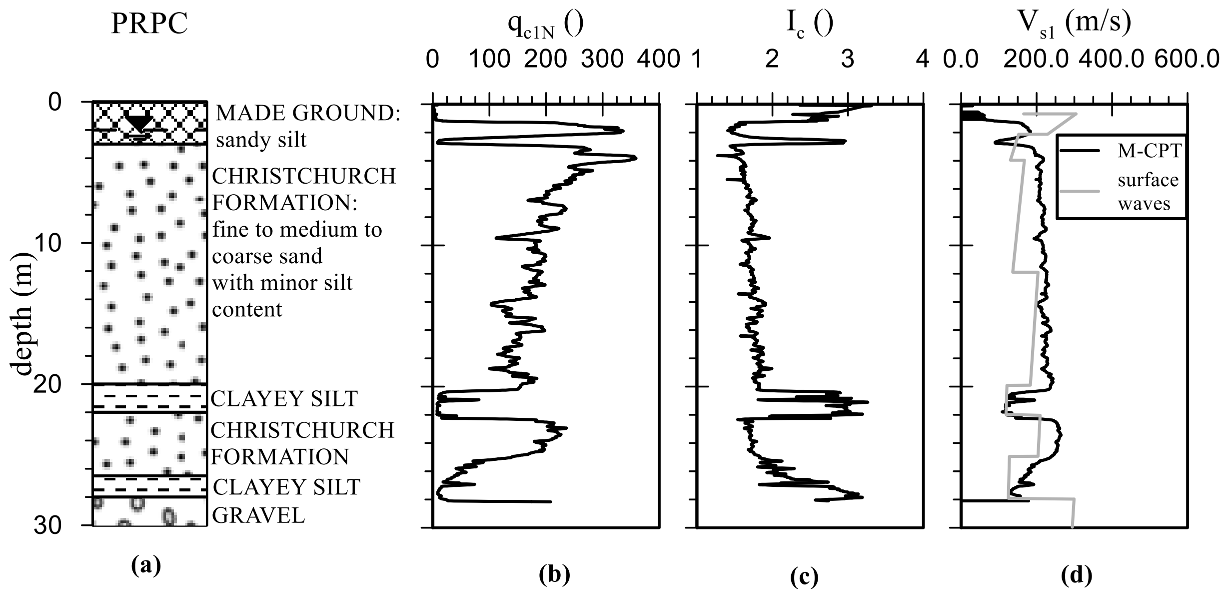

Figure 1: SMS PRPC (a) Summary borehole, (b) normalised CPT penetration resistance, q_{c1N}, (c) soil behaviour type index, I_c, (Robertson & Wride, 1998) (d) overburden-stress corrected shear wave velocity, V_{s1}, profiles (NZGD, 2016; Wotherspoon *et al.*, 2015)

Given the absence of direct measurements of shear wave velocity, V_s, at PRPC, surface wave measurements from Wood *et al.* (2011) and a Christchurch-specific CPT-V_s correlation - denoted as M-CPT - (McGann *et al.*, 2014) were used to infer the small strain shear stiffness profile at PRPC. Despite the uncertainty of the two methodologies, the two profiles match reasonably well (Figure 1d). GWT levels at PRPC were found to be between 1 to 2 m depth (Van Ballegooy *et al.*, 2014).

The appropriate characterisation of the in-situ void ratio is of fundamental importance, if meaningful simulations using a state parameter-based constitutive model are to be conducted. The expressions suggested by Baldi *et al.* (1986), Jamiolkowski *et al.* (2003), Robertson & Cabal (2012) (as cited in Green *et al.* (2014)), Kulhawy & Mayne (1990) and Lunne & Christoffersen (1983), were used to estimate the in-situ relative density, with Figure 2 showing the resulting profiles at PRPC. The observed differences arise mainly from the fact that the various expressions are based on sands of different compressibility, which has a significant effect on the cone resistance of a sand (Lunne *et al.*, 1997). The Jamiolkowski *et al.* (2003) correlation, developed based on calibration chamber tests on sands of a similar compressibility to those of Christchurch (low compressibility Toyoura sand and medium compressibility Ticino and Hokksund sand), was chosen for the analyses, resulting in an average D_r of about 70% across the sand layers.

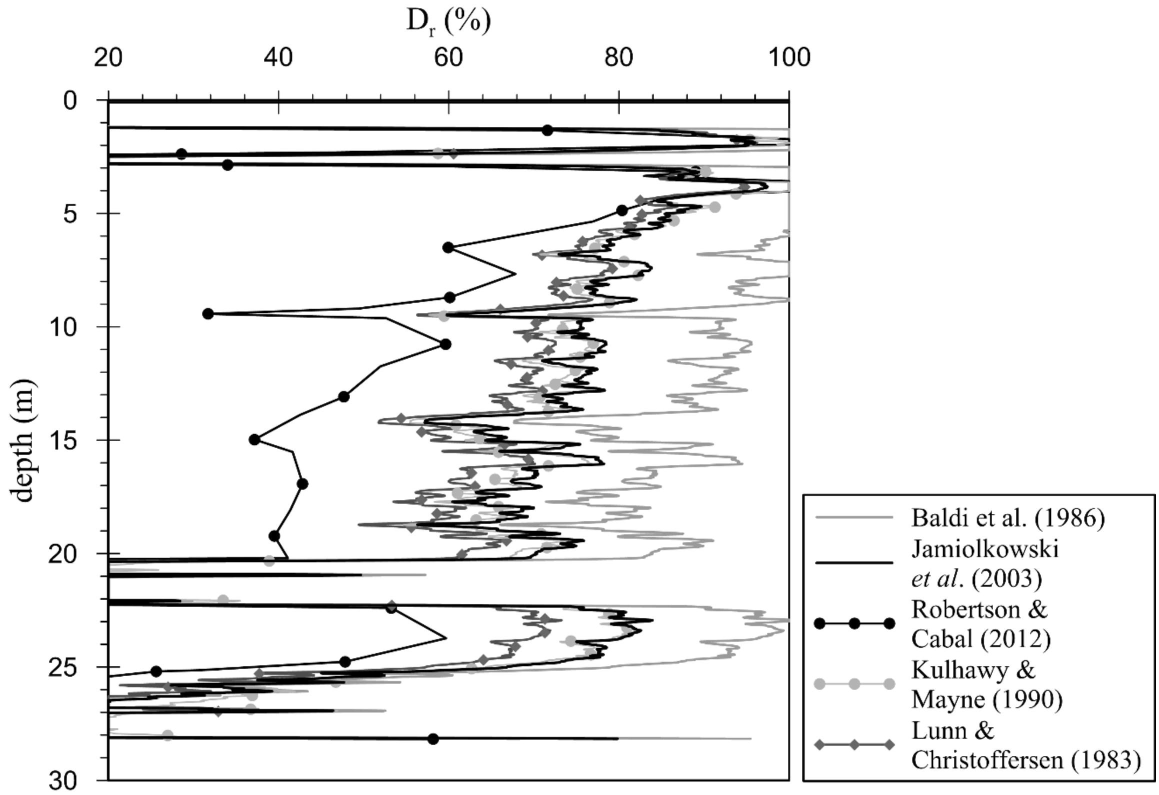

Figure 2: Relative density profile with depth for the sand layers at PRPC as obtained through CPT-D_r correlations

3 Constitutive models and site-specific calibration

3.1 Advanced Bounding Surface Plasticity Model for liquefiable strata

Amongst the various types of constitutive models developed for cyclic loading of granular soils (e.g. Prevost, 1978; López-Querol & Blazquez, 2006), bounding surface plasticity has been central in the field of geotechnics in modelling complex phenomena (e.g. Manzari & Dafalias, 1997; Papadimitriou & Bouckovalas, 2002; Dafalias & Manzari, 2004; Andrianopoulos *et al.*, 2010; Boulanger & Ziotopoulou, 2013; Taborda *et al.*, 2014; Dafalias & Taiebat, 2016; Amorosi *et al.*, 2018). The mechanical behaviour of sand is modelled herein with a bounding surface plasticity model (BSPM) based on Manzari & Dafalias (1997), modified for cyclic and dynamic solicitations (Papadimitriou & Bouckovalas, 2002). The model was further modified and implemented in ICFEP in three-dimensional stress space (Taborda, 2011; Taborda *et al.*, 2014). The recent modifications to the spherical part of the flow rule and the tensor representing the evolution of particle contact normal (i.e. soil fabric), as implemented and described by Tsaparli (2017), have also been utilised in this study for an improved prediction of cyclic strength, as well as realistic compliance post-unloading following a dilative response. The modified model formulation is summarised in Appendix A.

The model consists of 32 parameters, the meaning of which is explained in Taborda (2011), Taborda *et al.* (2014) and Tsaparli (2017). Monotonic and cyclic triaxial testing conducted by Taylor (2015) on undisturbed Gel-Push (GP) and reconstituted moist-tamped (MT) sand specimens from two CBD sites, designated as K1 and FBM, as well as bender element tests by Arefi (2014) on MT specimens from FBM were utilised for the calibration process. The surficial stratigraphy at both sites, summarised in Appendix B, is characteristic of the Christchurch's CBD, with the Christchurch Formation clean sands underlying station PRPC appearing here below about 8 m depth. An examination of the field shear wave velocities at the two sites (K1 and FBM) showed similar V_s values within the Christchurch Formation with that at PRPC ($V_{s1} \approx 200$ m/s) – see Appendix B. Tables B-1and B-2 in the appendix present the types of field tests that were available in the vicinity of the two sites, as well as the samples and available element testing, while average gradation and index properties of the sample types retrieved from the K1 and FBM sites and used for the BSPM calibration are presented in Table B-3.

For the calibration of the BSPM, the hierarchical approach presented in Loukidis & Salgado (2009), modified to account for the new flow rule for accurate modelling of cyclic strength (Tsaparli, 2017), was followed. The calibration of the BSPM for a natural soil, which can exhibit larger scatter in its response (e.g. critical state, G_{max}, dilatancy, cyclic strength etc) due to its very variable nature, as it is sourced from different depths, has different FC and may be characterised by different origin as in this case (i.e. alluvial/marine), versus calibrating the model for a particular fraction of sand, as it is often done, was found to require critical engineering judgment. Additionally, the calibration aimed at reproducing a model performance which would capture both the laboratory and field trends in a consistent manner. The calibration comprised an iterative process in which the model parameters were re-adjusted, when necessary, to fit the in-situ field values. This involved:

1. Increasing the B value in the G_{max} expression (Equation 1) from a value of 420.0, as calibrated based on bender elements on GP samples (Figure 3a), to a value of 500.0 (Figure 3b) to better fit the V_s measurements from downhole tests (DH) and CPT correlations in K1.

$$G_{max} = \frac{B \cdot p'_{ref}}{0.3 + 0.7 \cdot e^2} \cdot \sqrt{\frac{p'}{p'_{ref}}} \qquad 1.$$

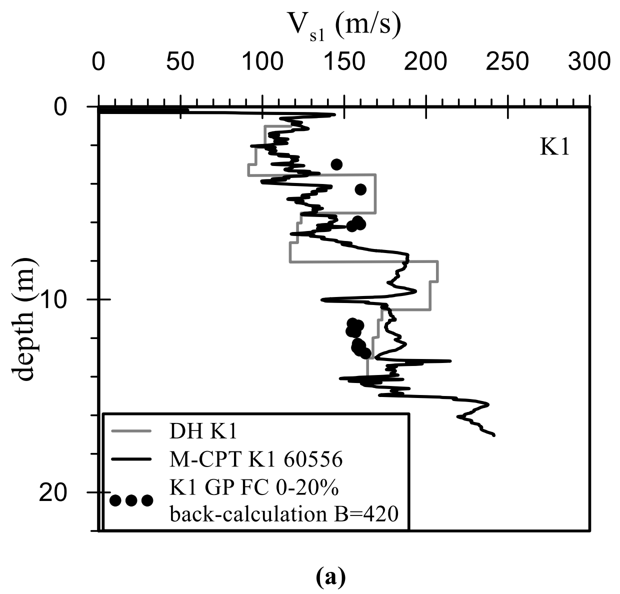

Figure 3: Back-calculation of V_s for the K1 GP samples for (a) a B of 420 based on bender element tests and (b) a B of 500 to better fit the downhole (DH) measurements (Taylor, 2015) and CPT_Vs (McGann *et al.*, 2014, M-CPT) correlations

2. Confirming the chosen CSL by comparing the in-situ state parameter values, ψ_0 (Been & Jefferies, 1985), of the GP samples from site K1 for a FC range of 0-20% against a CPT-ψ correlation (Robertson, 2012), to reinforce confidence in the chosen calibration (Figure 4).

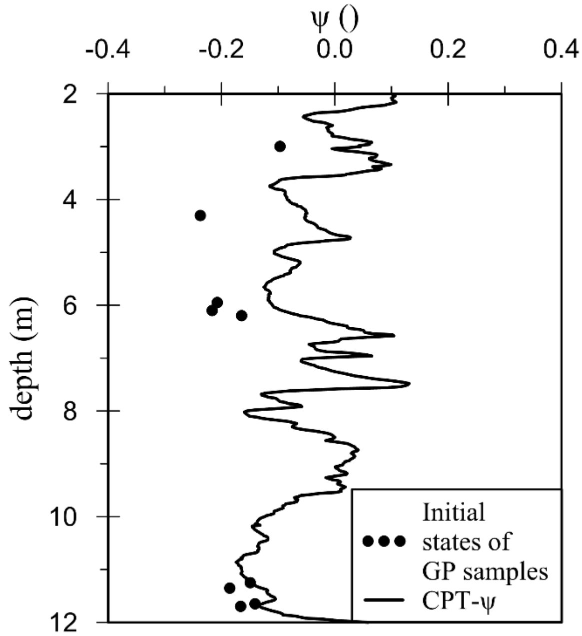

Figure 4: Comparison of the initial states of the GP samples with FC 0-20%, as obtained for the calibrated CLS of this study, with a CPT-ψ correlation for the K1 site based on Robertson (2012)

3. Adopting the cyclic resistance ratio (CRR)-penetration resistance trend by Idriss & Boulanger, (2008) to ensure that a reasonable field cyclic response with increasing effective stress is simulated, given the lack of adequate laboratory data to obtain a complete description of the overburden correction factor, K_σ (Ishihara, 1996). Figure 5 shows that the new formulation presented in Tsaparli (2017) results in a very good fit with empirical and laboratory trends.

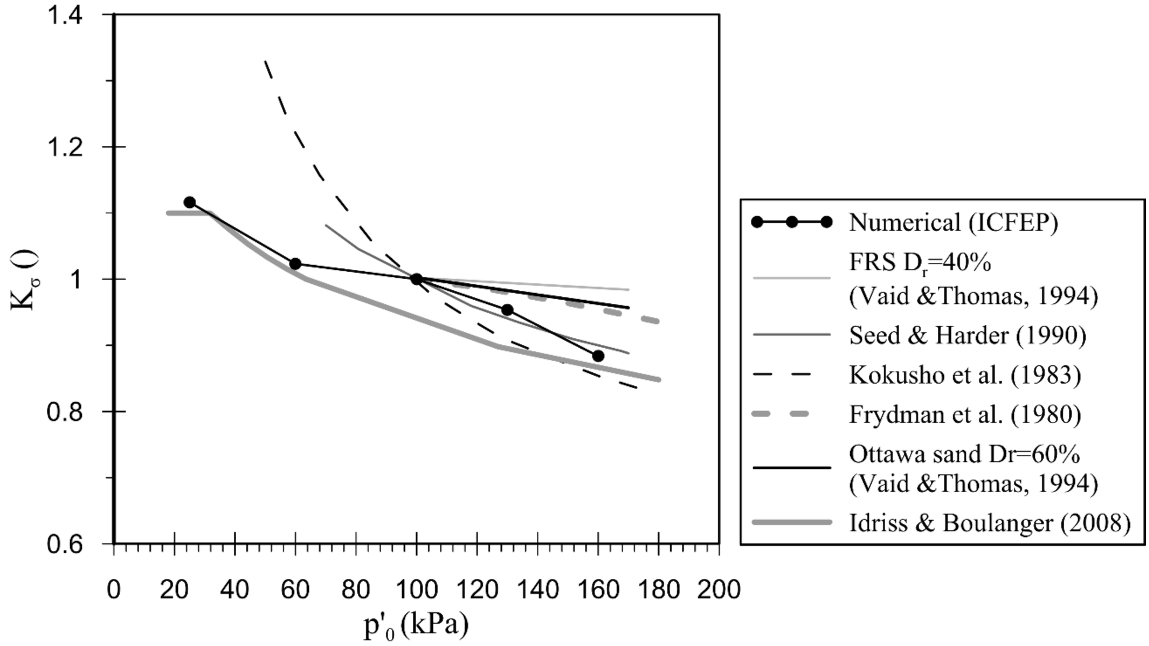

Figure 5: Computed K_σ trend of Christchurch sand for cyclic simple shear conditions for a D_r of 70% and comparison with available laboratory and field data (Vaid & Thomas, 1994; Seed & Harder, 1990; Kokusho *et al.*, 1983; Frydman *et al.*, 1980; Idriss & Boulanger, 2008)

The calibration presented above is valid for the Christchurch Formation sands with a FC of 0-20%, which are representative of the sands present at station PRPC.

Table 1 below summarises the physical properties of the sand unit, while Table A-2 in Appendix A presents the full set of parameters for the BSPM. The selection of the permeability coefficient was based on Taylor's (2015) estimates (Hazen, 1892; Kozeny, 1927; Carman, 1956), while for the earth pressure coefficient at-rest, K_0, the widely used approximation of Jaky (1944) was used:

$$K_0 = 1 - \sin\varphi'_{CS} \qquad 2.$$

Table 1: Properties of Christchurch sand with FC 0-20%

Model	Value	Model	Value
e_0	0.7336	Bulk unit weight, γ_b below GWT (kN/m^3)	19.50
Average minimum void ratio, e_{min} (Taylor, 2015)	0.6016	Permeability, k (m/s) (Taylor, 2015)	1.00E-04
Average maximum void ratio, e_{max} (Taylor, 2015)	1.0416	Earth pressure co-efficient at rest, K_0	0.44

The performance of the BSPM in element testing under monotonic and cyclic loading triaxial conditions is shown in Figures A-1 and A-2 in Appendix A, demonstrating that the model can capture the response of different initial states with a single set of calibrated model parameters. The stiffness degradation and damping variation curves as reproduced by the model during drained cyclic single element simple shear testing (10th loading cycle) with initial conditions corresponding to the middle of the thick sand layer at PRPC (i.e. 11.5 m depth) and at the field relative density of 70% are presented in Figure A-3. The corresponding Darendeli (2001) curves for the 10th loading cycle and a frequency of 1 Hz are superimposed in the figure for comparison purposes, showing a remarkable agreement in terms of stiffness degradation along the entire strain range. The damping variation is also predicted very accurately in the middle range of strains, though underprediced at very small strains due to the Masing-type formulation within the yield surface (Papadimitriou & Bouckovalas, 2002). Underprediction of damping at the small strain range is a well-known limitation of Masing-type cyclic models (Taborda & Zdravković, 2012). In the large strain range the damping ratio predicted by the model increases to larger values than those shown by Darendeli (2001). However, most element testing, including the database used by Darendeli (2001), is limited to strain levels of 1%, rendering the response at higher strain levels unknown.

3.2 Cyclic non-linear model for non-liquefiable strata

To model the silty/clayey layers, the Imperial College Generalised Small Strain Stiffness model - ICG3S - (Taborda & Zdravković, 2012; Taborda *et al.*, 2016), a cyclic non-linear model based on a modified hyperbolic function for the backbone curve, was utilised. This was calibrated on the basis of Darendeli (2001) for the 10^{th} loading cycle and a frequency of 1 Hz. To simulate material damping at very small strain levels, the novel varying scaling factor of Taborda & Zdravković (2012) has been adopted. More details of the model and model parameters can be found in the original references.

Given the lack of site-specific data for these layers, CPT correlations for fine grained soils and general trends found in the literature (Lunne *et al.*, 1997) were used to infer the plasticity index, PI, the overconsolidation ratio, OCR, the earth pressure coefficient at-rest, K_0, the bulk unit weight and the porosity. These are summarised in Table 2, while the calibrated ICG3S model parameters are presented in Table A-3. Small strain shear modulus, $G_{max,}$ values were assumed constant across these layers and were obtained from surface wave profiles (Wotherspoon *et al.*, 2015), validated against CPT-G_{max} correlations (Lunne *et al.*, 1997). The Darendeli curves and calibrated curves for each layer are plotted in Figure 6.

Table 2: Properties of clayey silt layers

Property	**Clayey sllt 0-3 m**	**Clayey silt 20-22 m**	**Clayey silt 26.5-28 m**
Plasticity index (%), PI	10.0	15.0	15.0
Overconsolidation ratio, OCR	5.0	2.0	2.0
Earth pressure co-efficient at rest, K_0	1.0	0.65	0.65
Bulk unit weight, γ_b, above GWT (kN/m^3)	17.0	N/A	N/A

Bulk unit weight, γ_b, below GWT (kN/m^3)	18.0	18.0	18.0
Mean effective stress, p'_0, at mid-depth (kPa)	30.0	165.0	210.0
Porosity, n	0.43	0.53	0.53
Permeability, k (m/s)	1.0E-07	1.0E-08	1.0E-08
Poisson's ratio, v	0.30	0.35	0.35

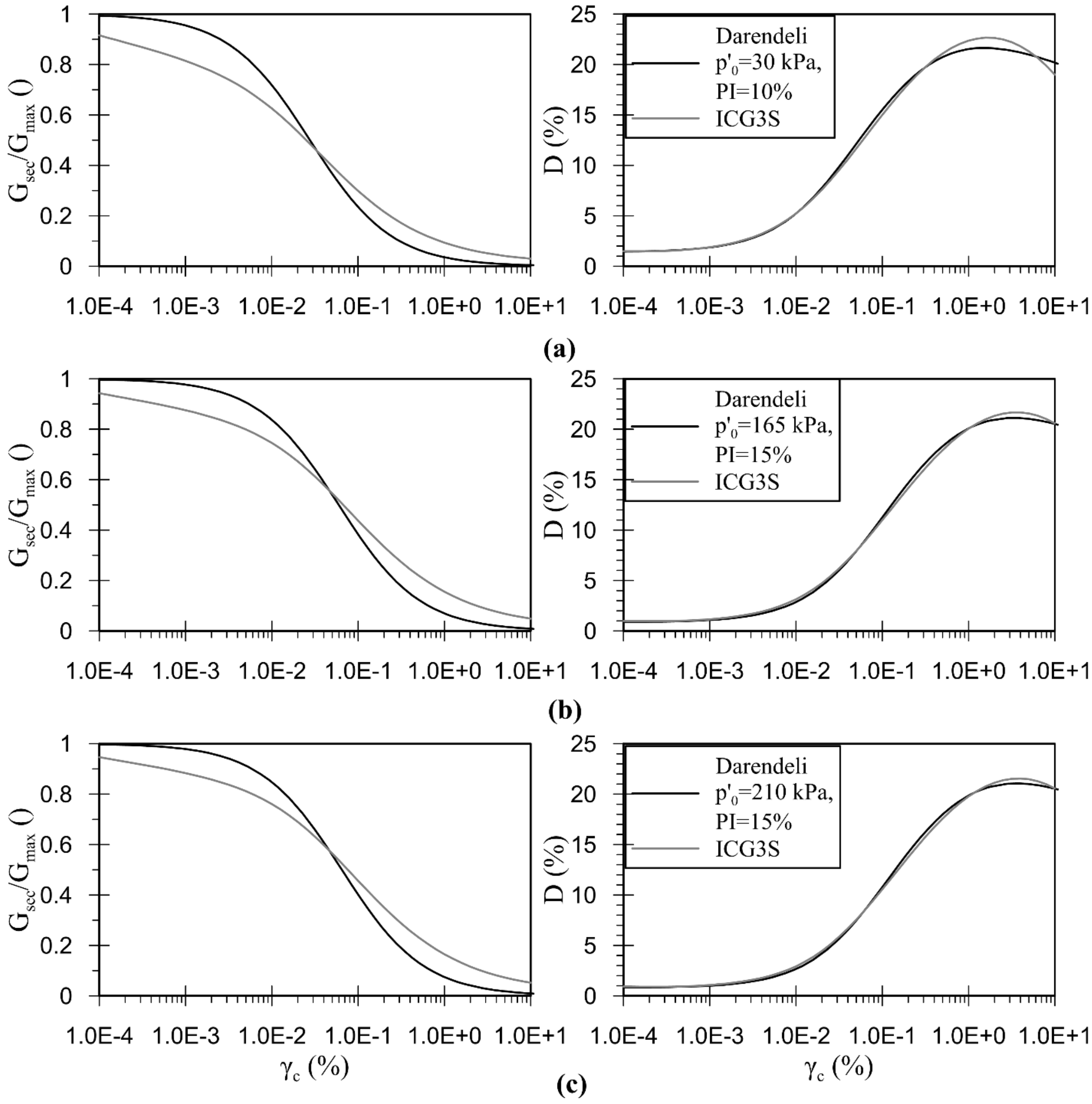

Figure 6: Darendeli (2001) normalised stiffness degradation and damping variation curves and ICG3S calibrated curves for the sandy/clayey silt layers at (a) 0-3 m, (b) 20-22 m and (c) 26.5-28 m depth

4 Selection of input ground motions

The selection of ground motion to be used as input in the FE analyses inevitably contributes to the various modelling uncertainties, due to the absence of downhole arrays in the wider CES area and the scarcity of outcrop rock records.

A possible candidate is the ground motion recorded at the Lyttelton Port Company station (LPCC), located at a distance of 4.8 km from the surface projection of the fault rupture (Bradley & Cubrinovski, 2011). This is the only station situated on engineering bedrock that recorded the Christchurch earthquake. The PRPC station is on the footwall, whereas the LPCC station lies on the hanging wall of the fault, and as a consequence the outcrop record could have been affected by amplifying hanging wall effects (Abrahamson & Silva, 1997). Therefore, a second record located on the footwall was also considered. Amongst the various available stations, the Riccarton High School station (RHSC), to the west of CBD, where gravelly deposits prevail below the ground surface and no significant non-linearity (in particular due to excess pore pressure development) is expected to have taken place, was considered appropriate.

The process of obtaining representative bedrock motions followed two main steps:

1. To account for non-linearity as a result of straining within any surficial softer deposits at the LPCC and RHSC stations, the motions were de-convolved to a reference depth of a stiffer formation. The deconvolution of the records was carried out with the frequency domain program EERA (Bardet *et al.*, 2000). Han (2014) and Han *et al.* (2018) showed that this can be employed for the vertical propagation of compressional waves, in a similar fashion to S-waves.
2. Furthermore, since both stations are at some distance from PRPC it is important to account for wave attenuation with distance. Therefore, the two deconvolved motions were scaled based on appropriate Ground Motion Prediction Equations (GMPE) prior to their use as input in the FE analyses modelling the PRPC station.

Further details of the procedure adopted can be found in Tsaparli (2017). It should be noted that, as the response within the stiff gravel is anticipated to be fairly linear (Smyrou *et al.*, 2011), bedrock outcropping instead of Riccarton gravel outcropping motions were calculated for the PRPC station based on the GMPE scaling. The ground motion was applied at the interface of the clayey silt layer at 28 m with the Riccarton gravel assuming engineering bedrock conditions. Given the high stiffness contrast between the clayey silt layer present between 26.5 and 28 m depth at PRPC and the modelled bedrock at that level, the calculated outcropping motion was considered appropriate for use as input in the numerical model at the base of the 28 m deep deposit (Kramer, 1996).

Table 3 presents the median and median ± one standard deviation (median ± SD) of outcrop PGA values for the largest horizontal component of PRPC. These are the PGA values to which the deconvolved LPCC and RHSC motions were scaled with the aid of GMPEs, to be used as input motions at the base of the mesh in the FE analyses modelling the PRPC station.

The GMPE of Bradley (2010) – denoted as B10 – and Campbell & Bozorgnia (2003) – denoted as CB03 – were utilised for the horizontal component. Bradley (2013) found the B10 model to perform well for the February Christchurch earthquake, while CB03 was used for comparison purposes. Finally, Table 4 presents the vertical motion predictions based on the Campbell & Bozorgnia (2003) – CB03 – and the Bozorgnia & Campbell (2016) - BC16 – GMPEs. The former was found by Lee *et al.* (2013) to perform well for the Christchurch earthquake, while the latter was again used to account for epistemic variability. Similar to the horizontal components, the vertical components from LPCC and RHSC were scaled to the predicted PGA values at PRPC (i.e. Table 4) prior to use as input motions in the FE analyses modelling the PRPC station. The single fault model of Beavan *et al.* (2011) was used to obtain the various characteristics of the fault rupture and the source-site distances, required as input in the GMPEs.

In total, 16 uni-directional analyses with the different input motions listed in Table 3 (horizontal motion only) and Table 4 (vertical motion only) were considered, while bi-directional analyses modelling simultaneously both modified components from stations LPCC or RHSC were additionally carried out.

Table 3: GMPE predictions of the largest outcrop horizontal PGA at SMS PRPC and summary of horizontal component FE analyses

Analysis ID / Input motion	Description	PGA (*g*)
LPCC S80W		
LS1	Median – SD PGA (B10)	0.264*g*
LS2	Median + SD PGA (B10)	0.849*g*
LS3	Median PGA (B10)	0.474*g*
LS4	Median PGA (CB03)	0.719*g*
RHSC N86W		
RN1	Median – SD PGA (B10)	0.271*g*
RN2	Median + SD PGA (B10)	0.871*g*
RN3	Median PGA (B10)	0.486*g*
RN4	Median PGA (CB03)	0.737*g*

Table 4: GMPE predictions of the outcrop vertical PGA at SMS PRPC and summary of vertical component FE analyses

Analysis ID / Input motion	Description	PGA (*g*)
LPCC UP		
LV1	Median – SD PGA (CB03)	0.295*g*
LV2	Median + SD PGA (CB03)	0.922*g*
LV3	Median PGA (CB03)	0.522*g*
LV4	Median PGA (BC16)	0.187*g*
RHSC UP		

RV1	Median – SD PGA (CB03)	0.295*g*
RV2	Median + SD PGA (CB03)	0.922*g*
RV3	Median PGA (CB03)	0.522*g*
RV4	Median PGA (BC16)	0.187*g*

5 Numerical aspects of finite element analyses

As aforementioned, the top 28 m of soil were modelled, down to the interface with the Riccarton gravel. The adopted stratigraphy and GWT level are shown in Figure 1a. Piezocone CPT tests (CPTu) in the vicinity of PRPC showed no presence of artesian pressures within the sandy strata and, as such, a hydrostatic pore water pressure was prescribed. Given the thicknesses of the various strata, as shown in Figure 1a, and their small strain elastic properties as described in the preceding sections, the natural non-degraded frequency, f_1, of the 28 m depth deposit for S- and P-wave propagation is equal to 1.633 and 14.640 Hz, respectively.

Non-linear elasto-plastic plane strain effective stress-based finite element (FE) analyses were carried out with ICFEP (Potts & Zdravković, 1999)). The coupling between the solid skeleton and the pore fluid was modelled using the u-p hydro-mechanical formulation (Zienkiewicz *et al.*, 1980). It should be noted that the problem under consideration is, for all values of soil permeability and for all ground motions and deposits considered, within the range over which the u-p formulation is valid (Zienkiewicz *et al.*, 1980).

To satisfy Bathe's (1996) recommendations for modelling frequencies up to about 30 Hz using 8-noded solid elements, an element size of 0.25×0.25 m^2 was adopted to ensure that waves of short wavelengths are not filtered out. For this, stiffness degradation due to cyclic straining was accounted for through a preliminary equivalent linear analysis. As a result of such analysis, a stiffness reduced to 20% of its small strain value was used in element size calculations, resulting in a mesh of a single column of 112×1 8-noded quadrilateral elements with pore water pressure degrees of freedom at the 4 corner nodes.

Tied degrees of freedom were employed at the lateral boundaries to ensure 1D soil response (Zienkiewicz *et al.*, 1988). Additionally, for the horizontal or vertical motion dynamic analyses the displacements were assumed to be zero at the base of the mesh in the vertical or horizontal direction, respectively, while no restriction of this kind was imposed for bi-directional dynamic analyses. The hydraulic regime in the soil column was defined through restricting the flow at the base of the mesh, a choice driven by the presence of the low permeability clayey silt layer at the interface with the gravel (see Figure 1a). Additionally, the pore water pressure degrees of freedom at the lateral nodes were tied to ensure 1D flow and drainage through the ground surface, while zero pore water pressure change was imposed at the top boundary. Finally, the acceleration time-history was applied incrementally at the bottom boundary.

In all analyses the non-linear solver is based on a modified Newton-Raphson scheme with a sub-stepping stress point algorithm (Potts & Zdravković, 1999), while the generalised α-method of Chung & Hulbert (1993) is used as the time-integration scheme with a spectral radius at infinity, ρ_∞, of 0.818 (Chung & Hulbert, 1993; Kontoe, 2006; Kontoe *et al.*, 2008; Han et al 2015a). The suitability of the CH scheme in analyses modelling the higher frequency vertical ground motion has been demonstrated in Tsaparli *et al.* (2017b). A time step of 0.004 s and 0.005 s was found adequate to ensure accuracy when the horizontal component of LPCC and RHSC, respectively, was used as input alone, but this had to be decreased to 0.003 s for vertical motion and bi-directional analyses, due to the wider frequency content of the input motions in the vertical direction.

It should be noted that, for brevity, only the results of selected analyses are presented in subsequent sections.

6 Horizontal motion analyses results

6.1 LPCC input motion

The results of analysis LS3, where the input motion was scaled to the median prediction of B10, are presented in this section. Figure 7a shows the input motion at the base of the mesh, while Figure 7b compares the computed ground surface acceleration time-history and Fourier Spectrum (FS) with those corresponding to the PRPC record (FS: Fourier amplitude, FA, versus frequency f). Soil non-linearity and stiffness degradation are evident from the early stages of loading through the high frequency attenuation and period elongation, with a pronounced peak appearing in the FS at a frequency of 0.732 Hz (Figure 7b).

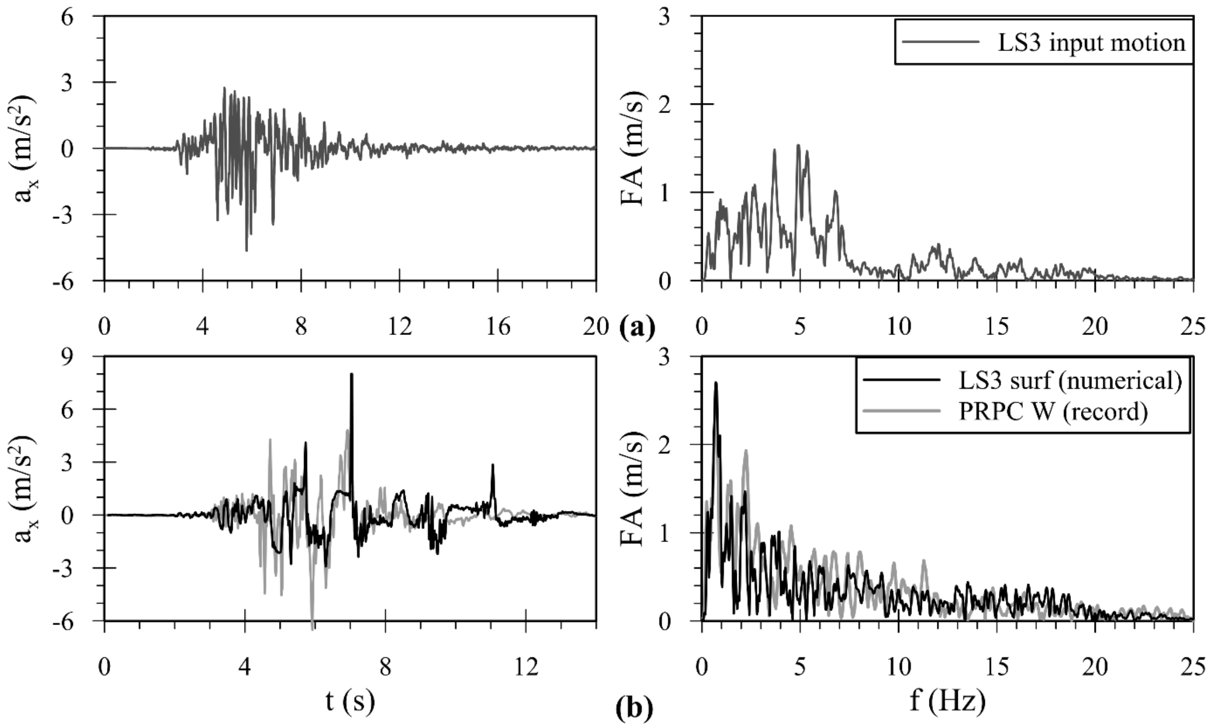

Figure 7: (a) Input motion for analysis LS3 and (b) comparison of computed ground surface acceleration time-history with the recorded East-West (W) ground surface motion at PRPC

It is obvious from Figure 7b that the computed ground surface response matches extremely well the recorded one. The FS shows that a very good fit has been achieved across the entire frequency content, with the highest peak at 0.732 s being captured accurately in terms of both frequency and amplitude. The occurrence of liquefaction is inferred from the amplitude drop at about 8.7 s, coinciding with the excess pore pressure ratio, r_u, exceeding a value of about 0.9 (initial liquefaction, Ishihara (1996)) at shallow depths within the thick sand layer (not shown herein for brevity). This is only slightly later compared to the recorded motion at about 7 - 8 s and it is followed by characteristic acceleration spikes indicating strain hardening during cyclic mobility. The computed acceleration time-history, however, does not exhibit the high frequency spikes that appear between 4.5 and 7 s in the record. It is likely that this discrepancy originates from differences in the bedrock acceleration, given the assumptions that had to be made, while heavy objects in the vicinity of PRPC (Tasiopoulou *et al.*, 2011) might have also affected the observed response.

6.2 RHSC input motion

The results of analysis RN1 (see Table 3) are shown in Figure 8. The predicted ground surface response is now significantly different from the recorded one, with significant period elongation taking place from about 6.5 s and liquefaction occurrence at about 11 s, as inferred from r_u time-histories at shallow depths within the sand layer ($r_u \geq 0.9$) despite the input motion having been scaled to the lowest bound PGA prediction (i.e. Median–SD PGA). Large cyclic mobility spikes govern the response thereafter. Despite possible hanging wall effects, the LPCC record, used in the previous section as input motion, appears to constitute a more representative outcrop motion than the deconvolved one at RHSC, at least in the horizontal direction. Bradley & Cubrinovski (2011) commented that, due to the steep angle of the fault dip (66.5°, Beavan, *et al.* (2011)), the amplifying hanging wall effect at LPCC was not expected to be significant.

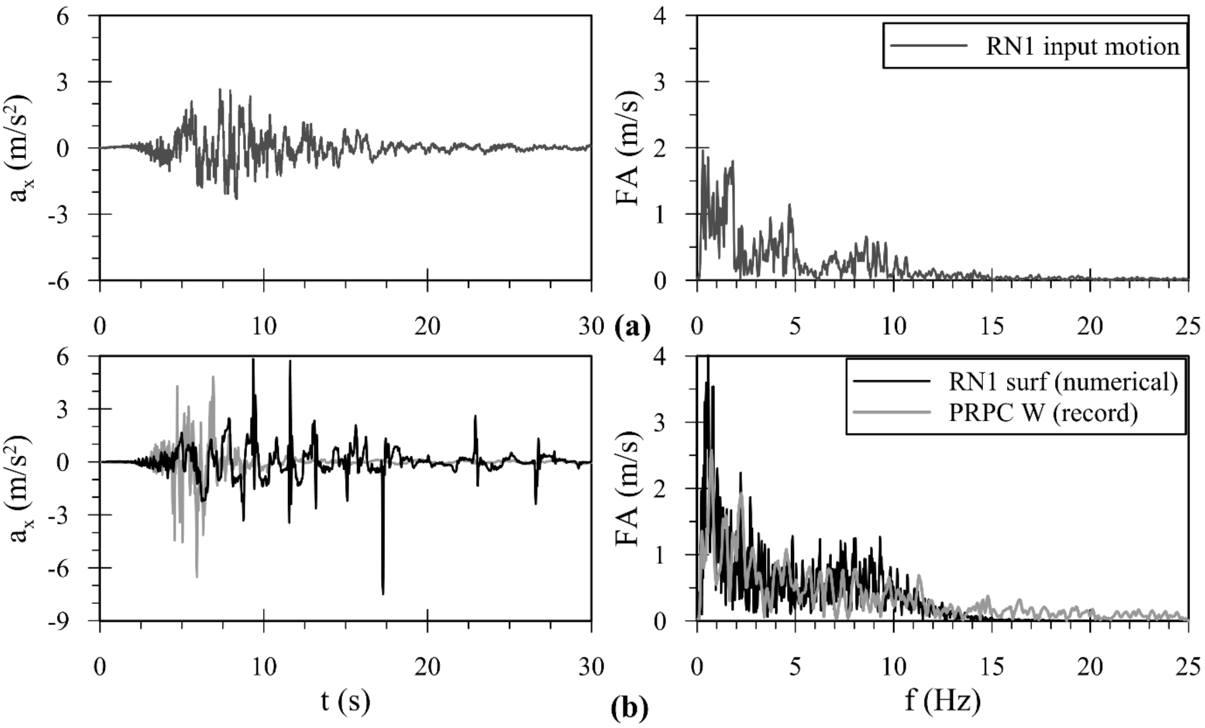

Figure 8: (a) Input motion for analysis RN1 and (b) comparison of computed ground surface acceleration time-history with the recorded East-West (W) ground surface motion at PRPC

7 Vertical motion analyses results

7.1 LPCC and RHSC input motions

The results of analysis LV1 are shown in Figures 9 and 10. It is evident that resonance and amplification take place at the (non-degraded) fundamental frequency of the deposit of about 14.6 Hz, resulting in an increase of the maximum acceleration from 2.9 m/s^2 at base to 10.12 m/s^2 at ground surface, which is, however, lower than the 15.98 m/s^2 measured at PRPC. Moreover, it appears that the effect of the higher fundamental frequency, as a result of neglecting the gravel layer down to bedrock, is much more dramatic compared to the horizontal motion. It is evident from the recorded FS that the components that should be amplified due to resonance correspond to frequencies of around 8 Hz rather than 14 Hz. The shape of the computed ground surface acceleration time-history is also very different to the recorded one.

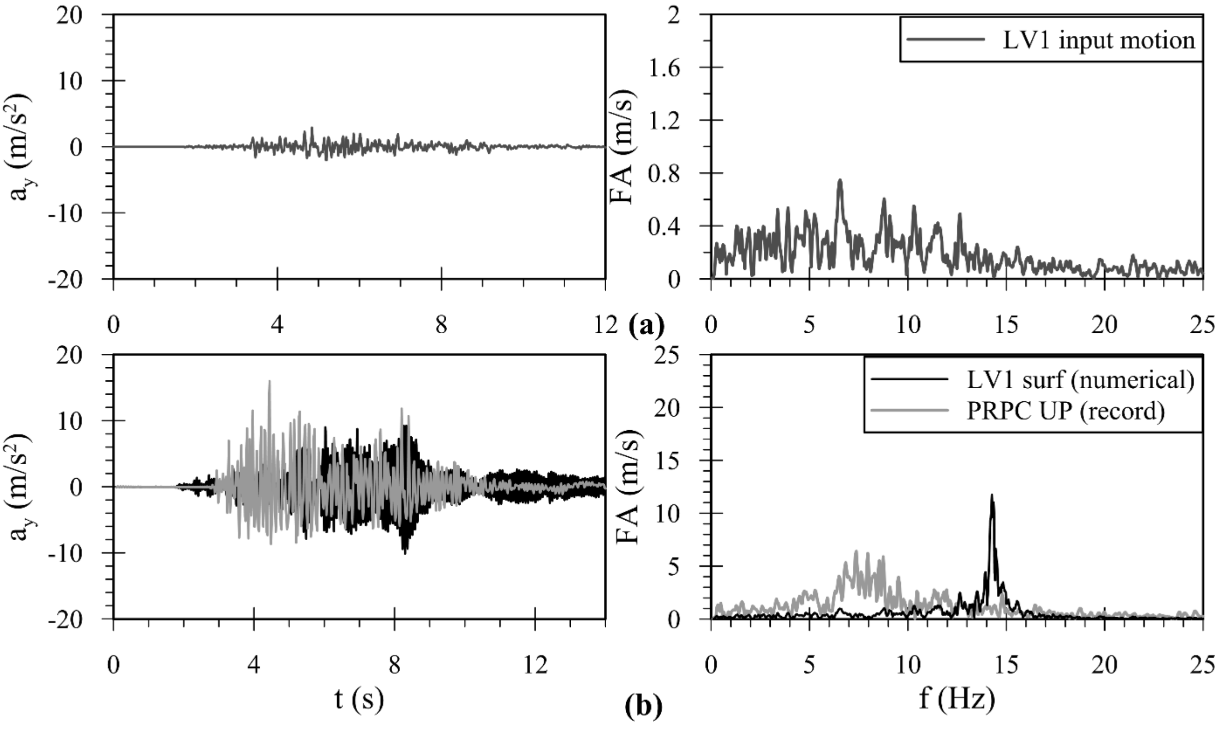

Figure 9: (a) Input motion for analysis LV1 and (b) comparison of computed ground surface acceleration time-history with the recorded vertical (UP) ground surface motion at PRPC

No plasticity is triggered in the analysis, with the mean effective stress profile remaining unaltered (Figure 10a)). The computed cyclic stress ratio (CSR) time-history (Figure 10b), calculated following the procedure outlined in Tsaparli *et al.* (2016) for vertical motion, is characterised by relatively low values, justifying the observed elastic response.

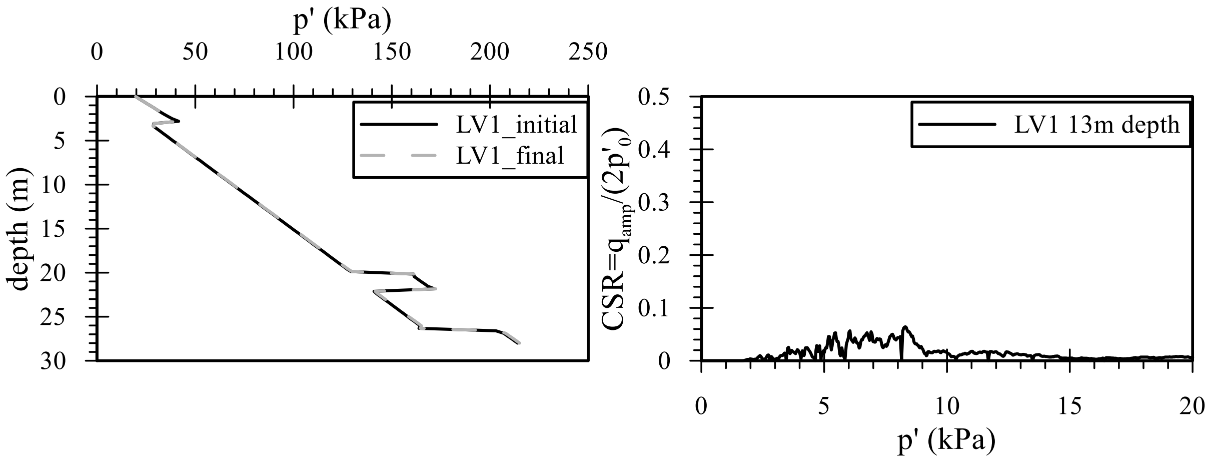

(a) **(b)**

Figure 10: (a) Initial and final (end of dynamic motion) mean effective stress profile and (b) CSR time-history at 13 m depth in the sand layer for analysis LV1

As expected, a similar discrepancy in the resonant frequency appears in analyses adopting the RHSC vertical component as input motion (Figure 11b). Nevertheless, the input motion is now characterised by higher amplitudes at a frequency range of 6.5 to 10 Hz, as it already incorporates any potential resonance effects within the gravel horizon.

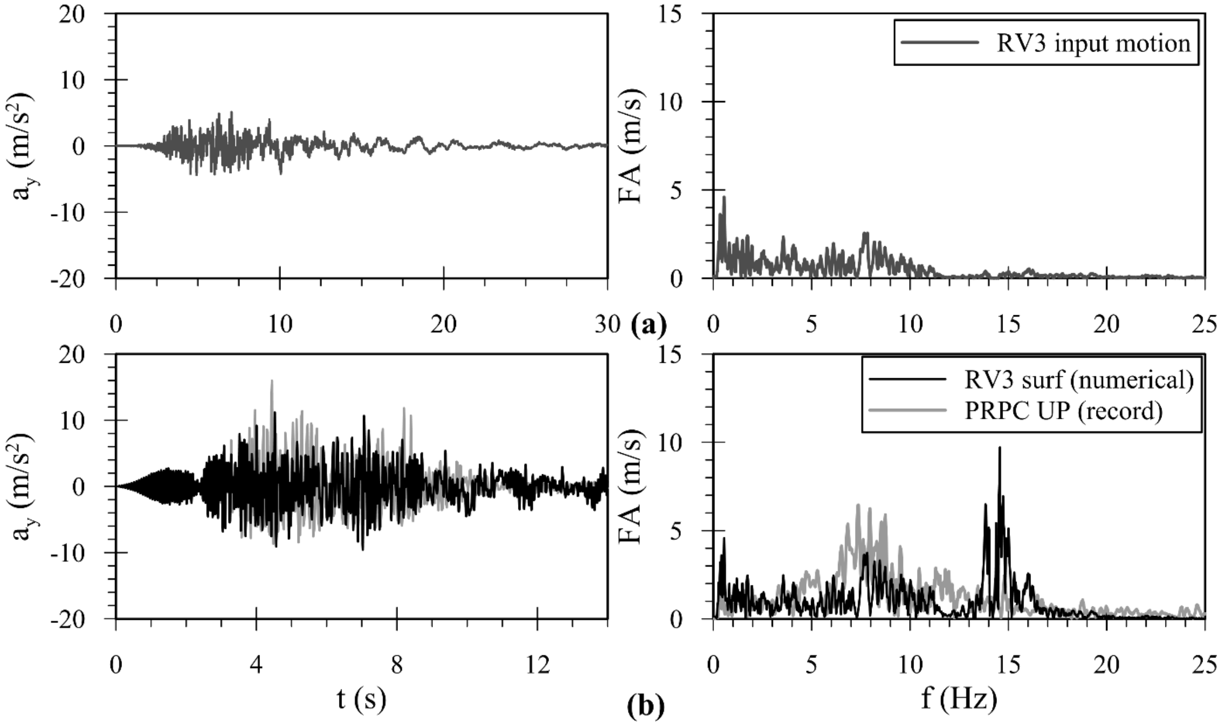

Figure 11: (a) Input motion for analysis RV3 and (b) comparison of computed ground surface acceleration time-history with the recorded vertical (UP) ground surface motion at PRPC

7.2 Finite element analyses modelling the Riccarton gravel horizon

Due to the impact of the fundamental frequency on the computed results in the vertical site response, an analysis was undertaken modelling the gravel at PRPC. The deep gravel horizon underlying Christchurch is interbedded with thin layers of silt, clay, peat and shelly sand (Brown *et al.*, 1995), however, for simplicity, a uniform gravel layer was modelled below 28 m depth. Surface wave measurements at the top of the Riccarton Gravel (Figure 1d) were compared against SPT-V_s correlations developed for gravels (Yoshida *et al.*, 1988) to infer G_{max} at that depth. SPT blow counts were adopted from tests conducted at RHSC for a depth corresponding to a similar initial vertical effective stress to that at the top of the Riccarton Gravel at PRPC (i.e. 28 m depth). Based on these and a gravel content of 50% (GNS Science, 2012), a V_s value of 350 m/s was adopted, resulting in a G_{max} at 28 m depth at PRPC of 250 MPa. The in-situ void ratio, e_0, was then back-calculated based on the relationship of Nishio *et al.* (1985), developed from reconstituted gravel specimens (Equation 3, Ishihara (1996)). Assuming a K_0 of 0.5 for the gravel layer, e_0 was found to be about 0.3, corresponding to a porosity of 0.23. These values were considered reasonable for gravel and, thus, were adopted for the subsequent analyses, where an assumption of constant void ratio with depth was made. As the exact thickness is not known, a total depth of 66 m was chosen as this was found to correspond to a fundamental frequency for the compressional mode close to 8 Hz, where the peak response in the recorded PRPC FS appears. This depth, however, is only indicative, since a number of simplifications, as described above, were made for the Riccarton gravel properties and composition. Modelling of the gravel layer in a more accurate manner is beyond the scope of this work. Additionally, the absence of sufficient testing on this soil layer means that the adoption of simplistic assumptions is required.

$$G_{max}\,(\text{kPa}) = 9360 \cdot \frac{(2.17 - e_0)^2}{1 + e_0} \cdot {p'_0}^{0.44} \qquad 3.$$

The gravel layer was also modelled as non-linear, using the ICG3S model, and with a permeability of 5.0E-02 m/s, based on the range reported by Lunne *et al.* (1997). Stiffness degradation and damping variation were based on the mean curve of Rollins *et al.* (1998), while the dimensions of elements, boundary conditions and time-step remained unaltered. The properties of this material are shown in Table 5, while the adopted ICG3S model parameters are presented in Appendix A, Table A-4.

Table 5: Properties of Riccarton gravel

Property	**Riccarton Gravel**
Earth pressure co-efficient at rest, K_0	0.50
Bulk unit weight, γ_b, below GWT (kN/m^3)	20.0
Mean effective stress, p'_0, at mid-depth (kPa)	315.20
Porosity, n	0.23
Permeability, k (m/s)	5.0E-02
Poisson's ratio, v	0.15

Results are presented only for the analysis using as input motion the LPCC vertical component scaled to the lower bound CB03 PGA prediction (Figure 12 - LV1_GR). The RHSC vertical motion already incorporates any potential resonance effects within the gravel layer, as previously explained, and in its present form cannot be used as input for analyses modelling the whole depth to bedrock.

The shift in the fundamental frequency from the value corresponding to the 28 m deep deposit (i.e. 14.6 Hz) to about 8.3 Hz, as shown from the FS in Figure 12, is evident. The prediction matches the recorded Fourier spectrum very well, at least in the frequency range where the peak response lies. The shape of the computed ground surface acceleration time-history is also now very similar to the recorded one, particularly on the negative side, though it fails to reproduce the individual high peaks noted on the positive (upward) side. Apart from differences in the input ground motion, the observed asymmetry might be a result of the trampoline effect, due to zero tensile strength arising from resonance and large vertical accelerations (Aoi *et al.*, 2008; Yamada *et al.*, 2009). No plasticity is once again predicted due to the vertical motion alone.

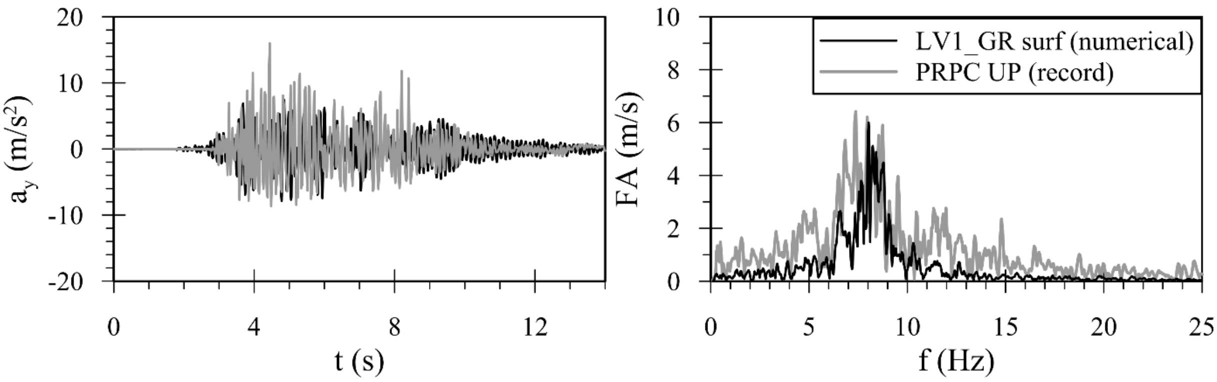

Figure 12: Comparison of computed ground surface acceleration time-history for analysis LV1_GR with the recorded vertical (UP) ground surface motion at PRPC

As aforementioned, in addition to the analyses listed in Tables 3 and 4, bi-directional analyses were also carried out modelling simultaneously the horizontal and vertical components of the earthquake. However, despite resonance taking place in the vertical direction, as the vertical component in this study did not result in high enough cyclic stress ratios for the modelled sand relative density at PRPC (i.e. D_r=70%) to invoke additional plasticity and excess pore pressures, the results of the bi-directional analyses in this particular case were very similar to those modelling the horizontal component only and are, therefore, not shown herein for brevity.

8 Effect of hydraulic regime

Numerical studies modelling level-ground liquefaction have shown that the velocity of flow needs to increase in order for the rate of co-seismic settlement to increase to levels observed in centrifuge testing (Manzari & Arulanandan, 1993; Arulanandan & Sybico, 1993; Muraleetharan, 1993; Balakrishnan, 2000; Coelho, 2007; Taiebat *et al.*, 2007; Su *et al.*, 2009; Andrianopoulos *et al.*, 2010; Taborda, 2011; Shahir *et al.*, 2014; Tsaparli *et al.*, 2016). Assuming that Darcy's law is valid, this implies that an increase in sand permeability takes place. A constant permeability 10 times larger than the original one (i.e. 1.0E-03 m/s) was assumed to approximate well the effect of liquefaction on this property (Shahir *et al.*, 2014; Tsaparli *et al.*, 2016). Additionally, to simulate a more realistic hydraulic regime, an analysis with a variable permeability model for the sand layers as a function of r_u, as shown in Figure 13, was conducted for the horizontal ground motion analysis LS3. This was done for the 28 m deep deposit, as modelling the stiff gravel horizon was not found to impact the findings in the horizontal direction, agreeing with the conclusions drawn by Smyrou *et al.* (2011). The properties of the remaining materials were kept unchanged.

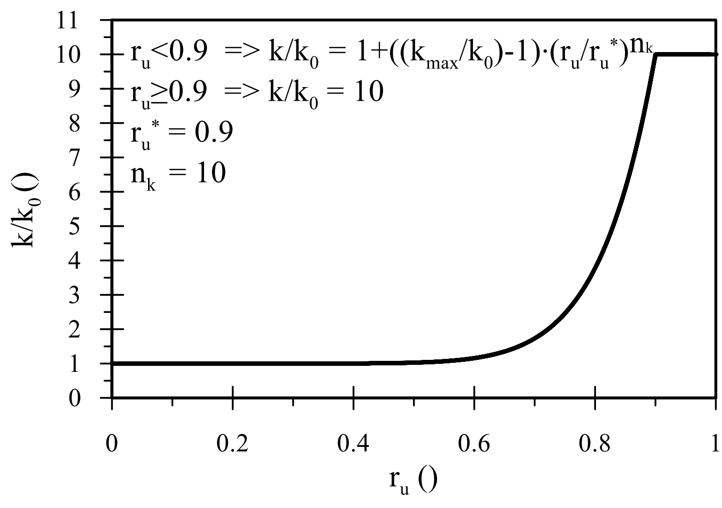

Figure 13: Modelled variation of permeability with excess pore pressure ratio

Figure 14 presents the maximum and final excess pore pressure ratio, r_u, profiles during the dynamic part for the original (LS3), higher constant permeability (LS3_k10^{-3}) and variable permeability analyses (LS3_Vk). For LS3_k10^{-3}, the higher co-seismic dissipation rate in the deeper layers due to the higher permeability results in a decreased maximum liquefaction depth compared to the original analysis (a criterion of $r_u \geq 0.9$ was adopted to determine this depth), reaching down to about 5.5 m instead of 6.5 m (Figure 14a). The greatest difference is observed at the end of the dynamic loading, where a quicker solidification process is noted due to the faster flow of water towards the interface with the silt layer at 3 m depth. However, the overall differences noted are not major. This agrees with the analytical solution of Biot's equations (Biot, 1941; 1956) by Zienkiewicz *et al.* (1980), which predict an undrained response for both LS3 and LS3_k10^{-3}. The presence of the low permeability silty layer at the top 3 m further prohibits the dissipation of excess pore water pressures from the ground surface.

Conversely, in the case of LS3_Vk, the predicted maximum liquefaction depth is similar to the original analysis (LS3), highlighting the difference between using a constant higher permeability and a more realistic variable function. The r_u profile at the end of the dynamic loading at shallow levels (Figure 14b), however, resembles the analysis LS3_k10^{-3}, implying that the permeability increases for a significant duration in LS3_Vk to allow for more flow of water to take place towards the top silt layer, as compared to analysis LS3. With increasing depth, the final r_u profile approaches the predictions of the original analysis LS3, as there has been insufficient build-up of pore water pressure at these deeper levels to result in an increase of permeability. Given that the difference in the predicted excess pore pressures between LS3 and LS3_Vk are not major, the computed ground surface acceleration response in LS3_Vk resembled the original analysis.

The computed liquefaction depth of 6.5 m contradicts the findings of the empirical assessment (Wotherspoon *et al.*, 2015). Tsaparli *et al.* (2018) validated the phenomenon of resonance in the vertical direction empirically through a comparison of the natural frequencies of the soil deposits underlying a number of SMSs in Christchurch with the predominant frequencies in the recorded ground surface response spectra. Through this they partly attributed this underperformance of the empirical assessment noted above to a potential plastic response resulting from the high vertical accelerations, further contributing to the excess pore pressures induced by the horizontal components.

Understanding the potential reasons behind the underperformance of the empirical procedure, however, has evolved since then through these more detailed site-specific FE analyses. The current analyses show that at least for the case of SMS PRPC, the inability of the empirical procedure to account for the co-seismic upward water flux, which forces the shallow sand layers to liquefaction despite their less contractive response, appears to be the main reason of the observed discrepancy. This is of profound importance as q_{c1N} values in the sand layer at shallow levels at PRPC are larger than 200 (Figure 1b), exceeding the q_{c1N} upper bound value in most design charts for liquefaction triggering assessment (Idriss & Boulanger, 2008). It is noted that resonance in the vertical direction could still constitute a potential reason for "false negative" predictions by the empirical assessment for other SMSs in Christchurch, particularly for those where the underlying sand layers are not as dense as those present beneath PRPC.

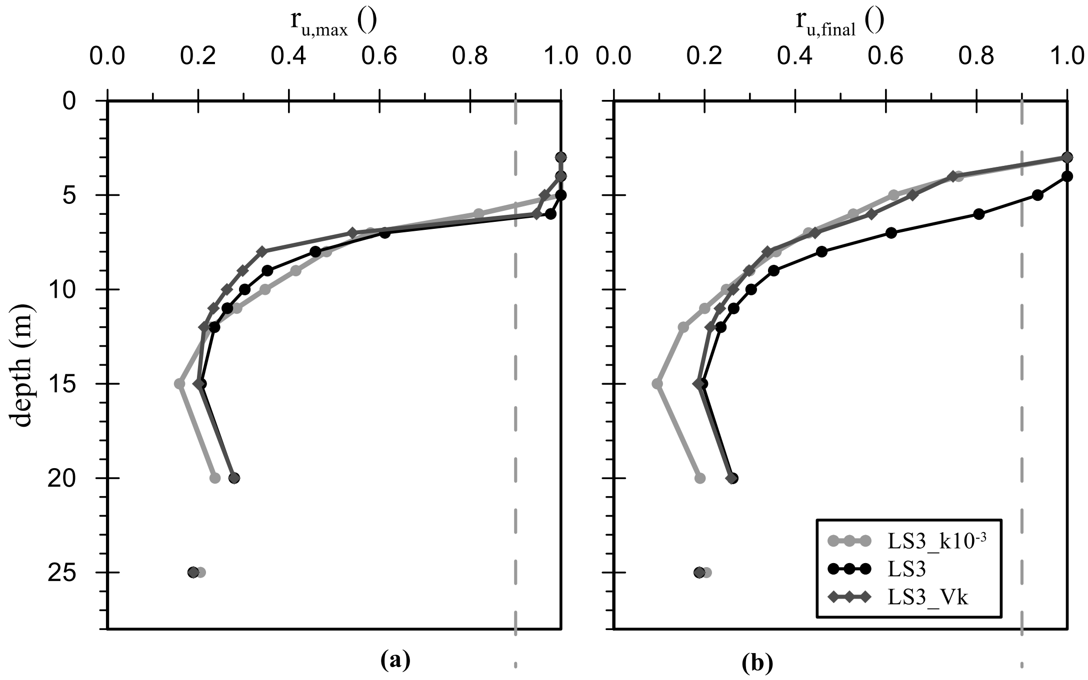

Figure 14: Profiles of (a) maximum and (b) final values of r_u within the sand layers during the strong motion for analysis LS3 with variable permeability (LS3_Vk). Results of analyses LS3_k10^{-3} (with constant higher permeability of 10^{-3} m/s) and original LS3 (with constant permeability of 10^{-4} m/s) are also shown for comparison purposes

Figure 15a shows the co-seismic settlements at ground level and immediately below the interface with the sand layer, using variable permeability. As soon as the permeability starts increasing, the higher upward water flux allows for more consolidation to take place within the sand layer (note the significant change in inclination at 3.25 m depth). Conversely, due to the much lower permeability of the top silt layer, hardly any drainage takes place through the ground surface, implying sand dilation immediately below the silt layer during dynamic loading. Figure 15b plots the total (co-seismic and post-consolidation) settlements: these indicate that, when the solidification process is over, settlements at 3.25 m depth have increased to 21 mm while ground surface settlements are smaller, in the order of 15 mm, due to the plastic sand dilation noted above.

It is believed that due to the co-seismic upward flow, large quantities of water pond below the base of the silt layer. For the continuity condition to stand, as water flowing into this 0.25 m thick sand zone cannot quickly seep through the low permeability silty layer and flow out of the deposit, part of it gets stored within these top elements of sand which exhibit a tendency for dilation. If the resulting hydraulic gradient between the base of the upper crust layer and the ground surface is large enough, then the pore water pressure within the sand layer will break through the crust resulting in fissuring and sand boiling (Ishihara, 1985). This latter effect is not modelled in the finite element analysis, as it involves the simulation of discrete features.

The results in terms of settlements obtained from the original analysis with a constant sand permeability of 1.0E-04 m/s (LS3) have also been superimposed in Figure 15 for comparison purposes. The difference arising from the two different hydraulic regimes is quite pronounced at the top of the sand layer (i.e.3.25 m depth) during the dynamic phase, as no increase in the permeability takes place in LS3 to allow for a larger co-seismic flow of water. Nevertheless, as the flow is very limited within the surficial clayey silt layer, the two analyses yield the same results at ground surface (0 m depth). In the long-term, since both analyses predicted similar amounts of excess pore water pressures and similar liquefaction zones (see Figure 14), total settlements are very similar.

It becomes apparent that for such cases where the overall hydraulic response is controlled by the presence of a surficial soil layer of low permeability, which restricts the flow of water towards the ground surface, the necessity for the use of such a non-linear variable permeability function in the analysis does not appear to be fundamental. This is opposite to the findings of Tsaparli *et al.* (2016) who examined a layer in which the excess pore water pressures could freely drain through the ground surface, showing that in such a scenario the use of a variable permeability model is required for the accurate simulation of liquefaction and ensuing solidification processes.

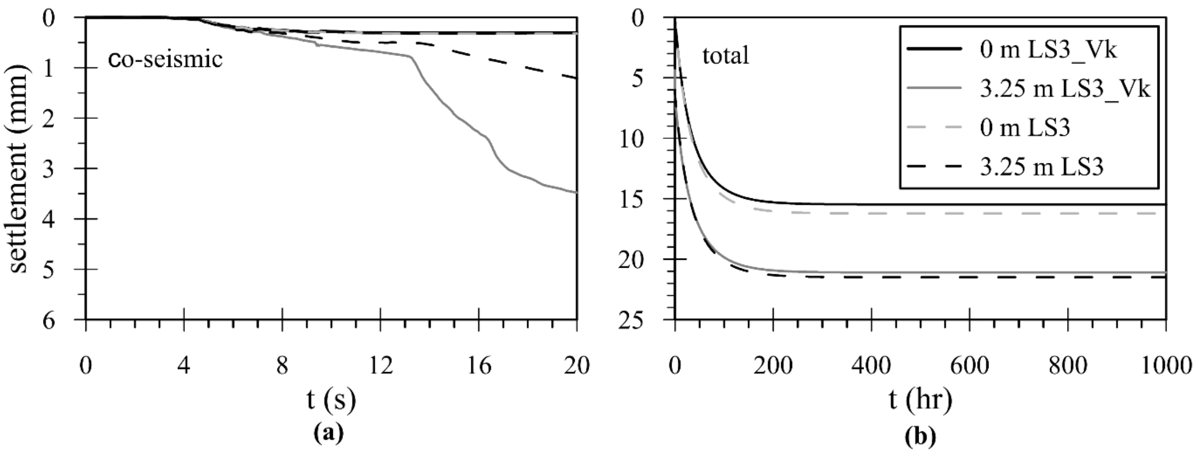

Figure 15: Predicted (a) co-seismic and (b) total post-liquefaction settlements at 0 and 3.25 m depth for analyses LS3 with variable permeability (LS3_Vk) and original analysis LS3 with constant permeability

It is of further interest to examine whether the above predicted results can actually lead to a breach in the top crust layer, resulting in ground surface manifestation of liquefaction, as observed after the February event (Wotherspoon *et al.*, 2015). Figure 16 presents the boundaries proposed by Ishihara (1985) for the prediction of ground surface manifestation of liquefaction as a function of the thickness of the surficial low permeability layer, the thickness of the underlying liquefied layer and the PGA. Superimposed on the graph is the prediction of the maximum liquefaction zone in analyses LS3 and LS3_Vk. Based on a PGA of 6.51 m/s^2, as recorded at PRPC, the numerical results do predict ground surface manifestation of liquefaction, in accordance with the observations (Wotherspoon *et al.*, 2015), as the point plots to the left of the boundary lines corresponding to smaller PGA values. Additionally, the total predicted settlements lie within the observed post-earthquake vertical movements (0.0 to 0.2

m, (NZGD, 2016)). Conversely, it is interesting to note that no ground surface manifestation of liquefaction was expected based on the empirical assessment results (Wotherspoon *et al.*, 2015).

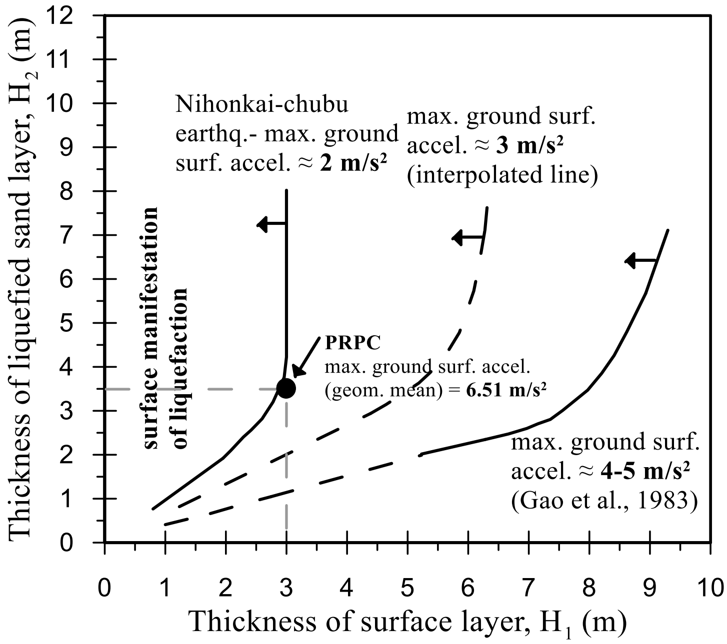

Figure 16: Proposed boundaries for the prediction of ground surface manifestation of liquefaction (adapted from Figure 88, Ishihara (1985))

9 Conclusions

A modified bounding surface plasticity model (Taborda *et al.*, 2014; Tsaparli, 2017), as well as a simpler cyclic non-linear model (Taborda *et al.*, 2016) were employed in this study to model the level-ground response of a SMS in Christchurch during the 22nd February 2011 M_w 6.2 seismic event. The station was of particular interest as it fell within the "false-negative" category, i.e. simplified procedures falsely predicted that no liquefaction would take place, which did not agree with field observations. It also registered surprisingly high vertical accelerations. Owing to the scarcity of outcrop rock records and the wave attenuation with distance, the motions recorded at two stations with no evidence of liquefaction were deconvolved and scaled, employing appropriate attenuation models, to then be used as input in the analyses.

The following conclusions can be drawn:

- The excellent agreement of the numerical predictions with the field observations demonstrates that, despite the numerous model parameters involved, many of which lack physical meaning, advanced constitutive models calibrated based on element testing can be successfully employed in predicting the field response. This requires careful calibration, such that the simulated mechanical response of sand is representative of the conditions prevailing in the field. This is a significant and novel contribution of this work as the capabilities of this type of constitutive model are often demonstrated for an artificially calibrated material tested under controlled conditions (e.g. centrifuge testing).
- The appropriate characterisation of the in-situ relative density is also of fundamental importance, if meaningful simulations are to be conducted using numerical models based on the state parameter framework. However, commonly employed correlations were shown to provide substantially different predictions of the in-situ material state.
- The reproduction of representative input ground motions remains one of the principal uncertainties when modelling case studies from the 2010-2011 CES. Deconvolution above the stiff gravel layer failed to provide realistic outcropping motions in this case.
- Modelling of the vertical site response was found to be more challenging compared to the horizontal direction, not only because of the lack of sufficient literature on the issue as well as soil characterisation data, but also due to the higher rate of wave attenuation with distance for the high frequency compressional waves. Most importantly, it was shown that a reasonable comparison with the vertical record can only be obtained when the total depth to bedrock is modelled, due to the phenomenon of resonance. This did not appear to have a substantial impact on the response in the horizontal direction, as the response of the deep gravel horizon between the surficial sandy strata and the bedrock was mainly linear elastic. As such, the theoretical scenario of resonance in the vertical direction, as introduced in Tsaparli *et al.* (2016; 2017a; 2018), was validated through comparisons with monitoring data.
- Finally, the conducted analyses also emphasise the importance of integrated numerical analysis in understanding limitations of empirically-derived correlations, highlighting the

non-conservative nature of widely used industry CPT liquefaction charts and the potential reasons behind it.

Appendix A

Appendix A presents the modified BSPM formulation, the calibrated model parameters for the Christchurch Formation sand with a FC of 0-20%, as well as examples of the performance of the BSPM against element testing. The calibrated model parameters for the cyclic non-linear ICG3S model are also included in the second part of the appendix.

Modified bounding surface plasticity model

Table A-1: Modified formulation of the two-surface BSPM (Tsaparli, 2017)

Descritpion		Equation	Parameters
Elastic behaviour			
Small strain shear modulus	A-1	$G_{max} = \frac{B \cdot p'_{ref}}{0.3 + 0.7 \cdot e^2} \cdot \sqrt{\frac{p'}{p'_{ref}}}$	B, p'_{ref}
Tangent shear modulus	A-2	$G_{tan} = \frac{G_{max}}{1 + \kappa \cdot (\frac{1}{a_{1}} - 1) \cdot (\frac{\chi^r_{ref}}{N_T \cdot \eta_1})^{\kappa - 1}}$	κ, α_1
	A-3	$\eta_1 = a_1 \cdot (\frac{G^{SR}_{max}}{p'^{SR}}) \cdot \gamma_1$	γ_1
Limit tangent shear modulus	A-4	$G_{tan} \geq \frac{G_{max}}{1 + \kappa \cdot (\frac{1}{a_1} - 1)}$	
Tangent bulk modulus	A-5	$K_{tan} = \frac{2 \cdot (1 + v)}{3 \cdot (1 - 2 \cdot v)} \cdot G_{tan}$	v
Model surfaces			
Critical State Line	A-6	$e_{CS} = (e_{CS})_{ref} - \lambda \cdot (\frac{p'}{p'_{ref}})^{\xi}$	$(e_{CS})_{ref}$, λ, ξ
Critical State surface	A-7	$\sqrt{3} \cdot \bar{J_2}^* = g(\theta, c) \cdot M^c_c \cdot p' \text{with } c{=}M^c_e/M^c_c$	M^c_e, M^c_c
Dilatancy surface	A-8	$\sqrt{3} \cdot \bar{J_2} = g(\theta, c) \cdot M^d_c \cdot p' = g(\theta, c) \cdot (M^c_c \cdot + k^d_c \cdot \psi) \cdot p'$	k^d_c
Bounding surface	A-9	$\sqrt{3} \cdot \bar{J_2} = g(\theta, c) \cdot M^b_c \cdot p' = g(\theta, c) \cdot (M^c_c \cdot + k^b_c \cdot \langle -\psi \rangle) \cdot p'$	k^b_c
Shape in the deviatoric plane	A-10	$g(\theta, c) = \frac{2 \cdot c}{i_1(\theta, c)} - i_2(\theta, c)$	
	A-11	$i_1(\theta, c) = \frac{1 + c}{2} - \frac{1 - c}{2} \cdot \cos(3 \cdot \theta + \frac{\pi}{2})$	
	A-12	$i_2(\theta, c) = \frac{1 + c}{2} + \frac{1 - c}{2} \cdot \cos(3 \cdot \theta + \frac{\pi}{2})$	
Primary yield surface	A-13	$F_1 = \sqrt{(\mathbf{s} - p' \cdot \boldsymbol{\alpha}) : (\mathbf{s} - p' \cdot \boldsymbol{\alpha})} - \sqrt{2/3} \cdot m \cdot p' = 0$	m
Gradient of the primary yield surface	A-14	$\frac{\partial F_1}{\partial \sigma'} = \mathbf{n} - \frac{V}{3} \cdot \mathbf{I_3}$	
	A-15	$V = \boldsymbol{\alpha} : \mathbf{n} + \sqrt{2/3} \cdot m$	
Secondary yield surface	A-16	$F_2 = p'_{YS} - p' = 0$	p'_{YS}
Gradient of the secondary yield surface	A-17	$\frac{\partial F_2}{\partial \sigma'} = \mathbf{I_3}$	
Unit stress ratio tensor	A-18	$\mathbf{n} = \frac{\bar{\mathbf{r}}}{\sqrt{2/3} \cdot m} = \frac{\mathbf{r} - \boldsymbol{\alpha}}{\sqrt{2/3} \cdot m} = \frac{\mathbf{s} - p' \cdot \boldsymbol{\alpha}}{\sqrt{2/3} \cdot m \cdot p'}$	
Image point of current stress ratio on the model surfaces	A-19	$\boldsymbol{\alpha}^{c,b,d} = \alpha^{c,b,d}_{\theta} \cdot \mathbf{n} = \sqrt{2/3} \cdot (g(\theta, c) \cdot M^{c,b,d}_c - m) \cdot \mathbf{n}$	
Distance of the current stress state from the model surfaces	A-20	$d^{c,b,d} = (\boldsymbol{\alpha}^{c,b,d} - \boldsymbol{\alpha}) : \mathbf{n}$	

Plastic behaviour-primary yield surface			
Flow rule	A-21	$\frac{\partial P_1}{\partial \sigma'} = \mathbf{n} + \frac{D}{3} \cdot \mathbf{I}_3 = \mathbf{n} + \frac{A_d \cdot d^d}{3} \cdot \mathbf{I}_3$	
	A-22	$A_d = A_0 + (A_{0,min} - A_0) \cdot (\frac{d^d}{d^{d,SR}})^b$	$A_0, A_{0,min}$
	A-23	$d^{d,SR} = (\boldsymbol{\alpha}^{\mathbf{d}} - \mathbf{r}^{\mathbf{SR}}): \mathbf{n}$	
	A-24	$\begin{cases} \text{if } p'_0 \geq p'_{0,A} \text{ then } b = d_1 \cdot \exp(d_2 \cdot p'_0) \leq b_{max} \\ \text{if } p'_0 < p'_{0,A} \text{ then } b = b_d + (\frac{p'_0}{p'_{0,A}})^{d_3} \cdot (b_l - b_d) \end{cases}$	$p'_{0,A}$, d_1, d_2, d_3, b_d, b_{max}
	A-25	$b_l = d_1 \cdot \exp(d_2 \cdot p'_{0,A})$	
Hardening modulus	A-26	$A = p' \cdot h_e \cdot h_g \cdot h_b \cdot h_f \cdot d^b$	
	A-27	$h_e = h_0 \cdot (1 - \gamma \cdot e) \geq h_0 \cdot (1 - \gamma \cdot e_{max})$	h_o, γ, e_{max}
	A-28	$h_g = G_{tan}^{\alpha_G}$	α_G
	A-29	$h_b = (\frac{p'}{p'_{ref}})^{\mu-1} \cdot (\frac{\lvert d^b \rvert}{\lvert d_{ref}^b - \lvert d^b \rvert \rvert})^{\beta+1}$	μ, β
	A-30	$d_{ref}^b = \sqrt{2/3} \cdot ((g(\theta, c) \cdot M_c^b - m) + (g(\theta + \pi, c) \cdot M_c^b - m))$	
	A-31	$h_f = \begin{cases} \frac{1 + \langle f_p \rangle^2}{1 + \langle \mathbf{f}: \mathbf{n} \rangle}, & \text{if } f_p \text{ is active} \\ \frac{1}{1 + \langle \mathbf{f}: \mathbf{n} \rangle}, & \text{if } f_p \text{ is disregarded} \end{cases}$	
Plastic behaviour-secondary yield surface			
Flow rule	A-32	$\frac{\partial P_2}{\partial \sigma'} = \mathbf{I}_3$	
Hardening modulus	A-33	$A_2 = 0.0$	
Hardening rules			
Axis of primary yield surface	A-34	$\Delta\boldsymbol{\alpha} = \langle \Lambda \rangle^{**} \cdot h_e \cdot h_g \cdot h_b \cdot h_f \cdot (\boldsymbol{\alpha}^b - \boldsymbol{\alpha})$	
Fabric tensor	A-35	$\Delta f_p = H \cdot \Delta\varepsilon_{vol}^p$	
	A-36	$\Delta\mathbf{f} = -H \cdot \langle -\Delta\varepsilon_{vol}^p \rangle \cdot [C_f \cdot \mathbf{n} + \mathbf{f}]$	C_f
	A-37	$H = H_0 \cdot (\frac{\sigma'_{1,0}}{p'_{ref}})^{-\zeta} \cdot \langle -\psi_0 \rangle$	H_0, ζ

*: $\bar{J}_2 = 1/2 \cdot \bar{r}:\bar{r}$

**< >: Macaulay brackets, $\langle x \rangle = x$ if $x > 0$ and $\langle x \rangle = 0$ if $x < 0$

Table A-2: BSPM model parameters for Christchurch sand FC 0-20%

Model parameter	**Value**	**Model parameter**	**Value**	**Model parameter**	**Value**	**Model parameter**	**Value**
$\mathbf{p'_{ref}}$ **(kPa)**	100.0	$\mathbf{A_0}$	1.00	**m**	0.065	$\boldsymbol{\gamma}$	0.629

$\mathbf{(e_{CS})_{ref}}$	0.99	$\mathbf{A_{0,min}}$	0.00	$\mathbf{p'_{YS}}$ **(kPa)**	1.00	$\mathbf{e_{max}}$	1.51
$\boldsymbol{\lambda}$	0.08	$\mathbf{p'_{0,A}}$ **(kPa)**	40.0	**B**	500.0	$\boldsymbol{\alpha}$	1.00
$\boldsymbol{\xi}$	0.54	$\mathbf{b_d}$	0.115	$\mathbf{a_1}$	0.375	$\boldsymbol{\beta}$	0.00
$\mathbf{M_c^c}$	1.395	$\mathbf{d_1}$	0.12	$\boldsymbol{\kappa}$	2.00	$\boldsymbol{\mu}$	1.00
$\mathbf{M_e^c}$	1.00	$\mathbf{d_2}$	1.83E-2	$\boldsymbol{\gamma_1}$	1.222E-03	$\mathbf{H_0}$	2000.0
$\mathbf{k_c^b}$	1.83	$\mathbf{d_3}$	6.50	$\boldsymbol{\nu}$	0.15	$\boldsymbol{\zeta}$	2.35
$\mathbf{k_c^d}$	2.21	$\mathbf{b_{max}}$	50.00	$\mathbf{h_0}$	0.179	$\mathbf{C_f}$	50.0

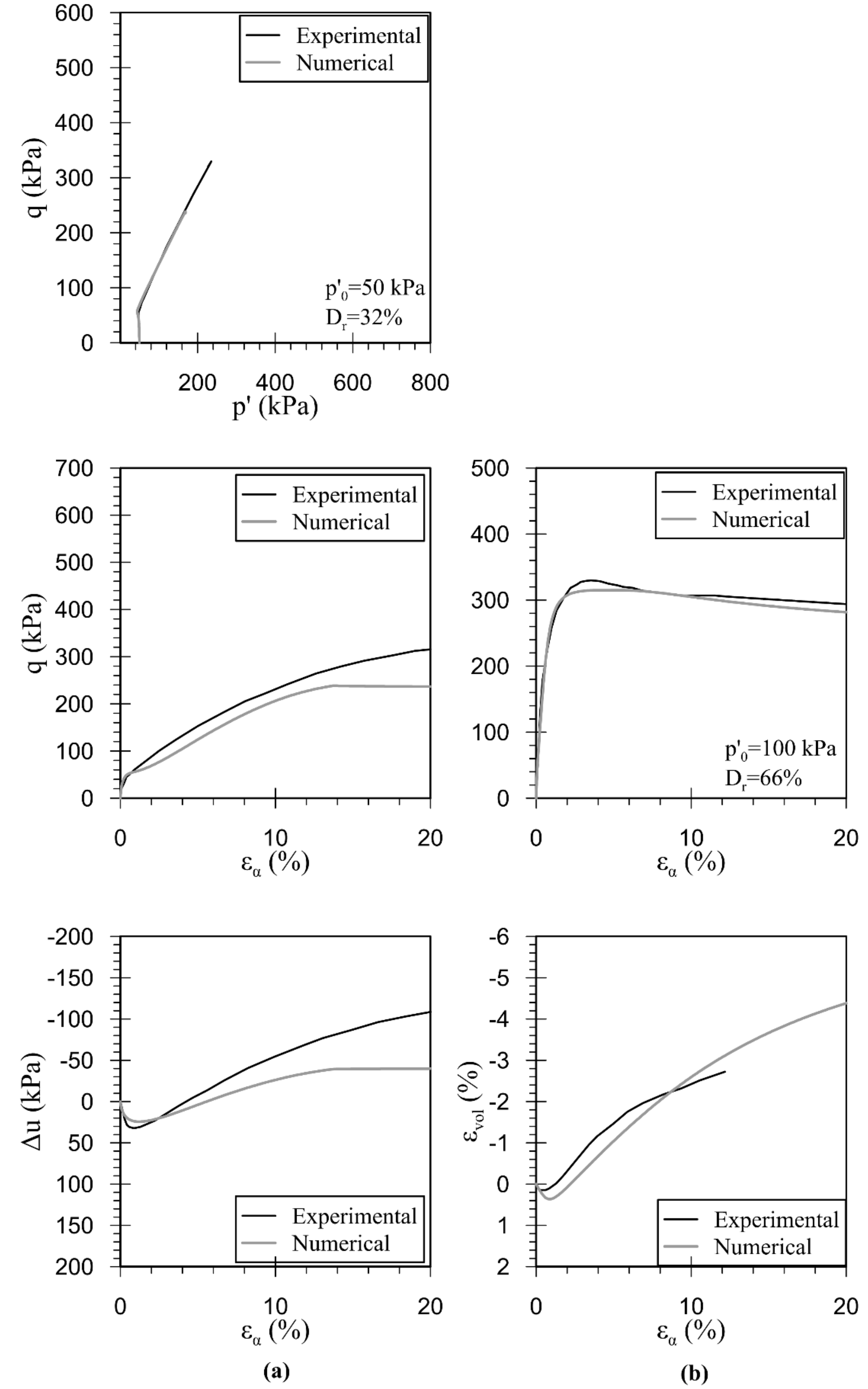

Figure A-1: BSPM performance in (a) undrained and (b) drained monotonic triaxial conditions

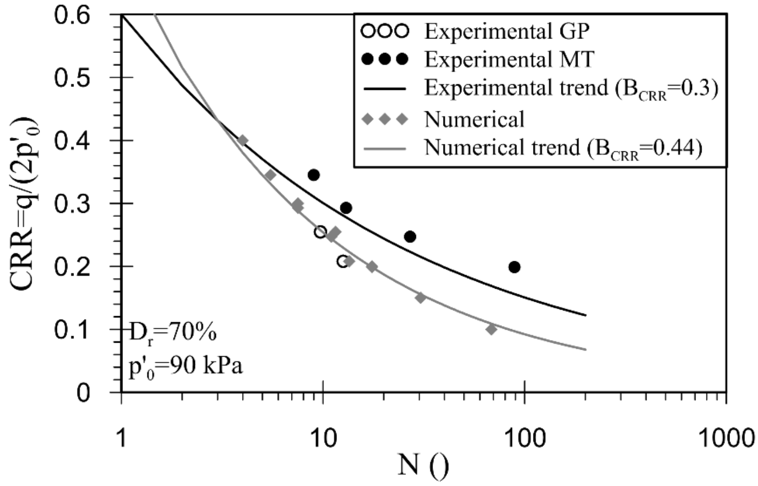

Figure A-2: BSPM performance in cyclic triaxial conditions (B_{CRR} is the slope of a power law fit to the cyclic strength data)

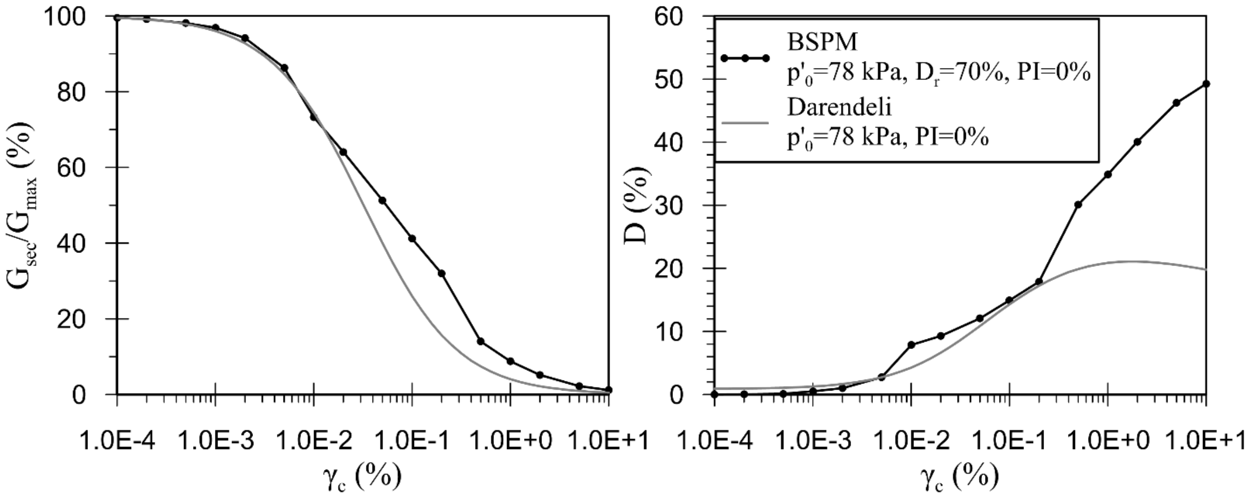

Figure A-3: Stiffness degradation and damping variation curves reproduced by the BSPM for initial conditions corresponding to the middle of the thick Christchurch sand layer at PRPC (i.e. 11.5 m depth) and to the field relative density, together with the corresponding curves based on Darendeli (2001).

<u>*Imperial College Small Strain Stiffness model*</u>

Table A-3: ICG3S model parameters for the clayey silt layers

Model parameter	Silt 0-3m	Silt 20-22m	Silt 26.5-28m
Maximum stiffness			
G_{max}	50852.0 kPa	46976.0 kPa	53032.0 kPa
Shear stiffness degradation			
$a_{0,c}$	1.0600E-4	0.2141E-3	0.2350E-3
$a_{1,c}$	0.0	0.0	0.0
$a_{2,c}$	0.0	0.0	0.0
$b_{0,c}$	1.076	1.056	1.061
$R_{G,min}$	0.0	0.0	0.0
G_{min}	1.0 kPa	1.0 kPa	1.0 kPa
Varying scaling factor			
$d'_{1,G}$	203.0796	105.8509	103.4601
$d''_{1,G}$	0.0	0.0	0.0
$d_{2,G}$	0.206176	0.194948	0.195534
$d_{3,G}$	9661.764	7017.649	6888.291
$d_{4,G}$	0.638378	0.652856	0.657224

Table A-4: ICG3S model parameters for the Riccarton gravel layer

Model parameter	Silt 0-3
Maximum stiffness	
G_0	71002.86
$f_G(e)$	$(2.17-e)^2/(1+e)$
p'_{ref}	100.0 kPa
m_G	0.44
v	0.15
Shear stiffness degradation	
$a_{0,c}$	1.111E-4
$a_{1,c}$	0.0
$a_{2,c}$	0.0
$b_{0,c}$	1.18
$R_{G,min}$	0.0
G_{min}	1.0 kPa
Varying scaling factor	
$d'_{1,G}$	451.990
$d''_{1,G}$	0.0
$d_{2,G}$	0.168
$d_{3,G}$	3267.26
$d_{4,G}$	0.52

Appendix B

Appendix B presents information on sites K1 and FBM from where sand samples were retrieved (Taylor, 2015; Rees, 2010; Arefi, 2014): Figures B-1 and B-2 present the stratigraphy at the two sites, Tables B-1 and B-2 summarise the available field tests, soils samples and element testing for each site, while Table B-3 tabulates the gradation and index properties of the samples types from sites K1 and FBM that were used in the calibration of the modified BSPM.

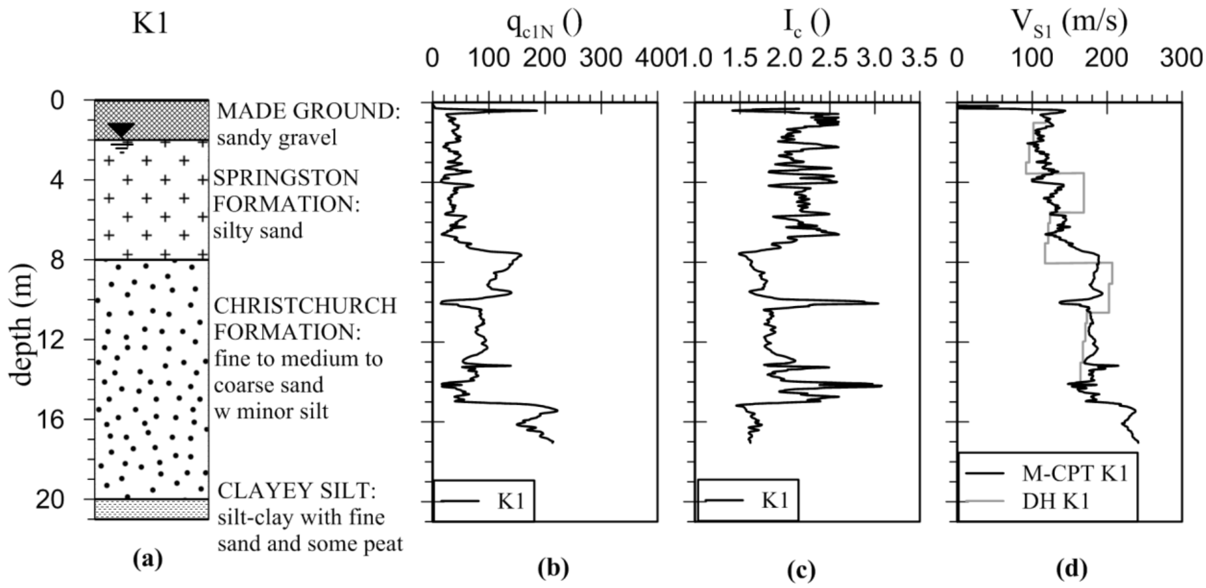

Figure B-1: K1 site (a) Summary borehole, (b) normalised CPT penetration resistance, q_{c1N}, (c) soil behaviour type index, I_c, (d) V_{s1} profile through CPT correlations (M-CPT) and downhole (DH) measurements (after Taylor, 2015; NZGD, 2016)

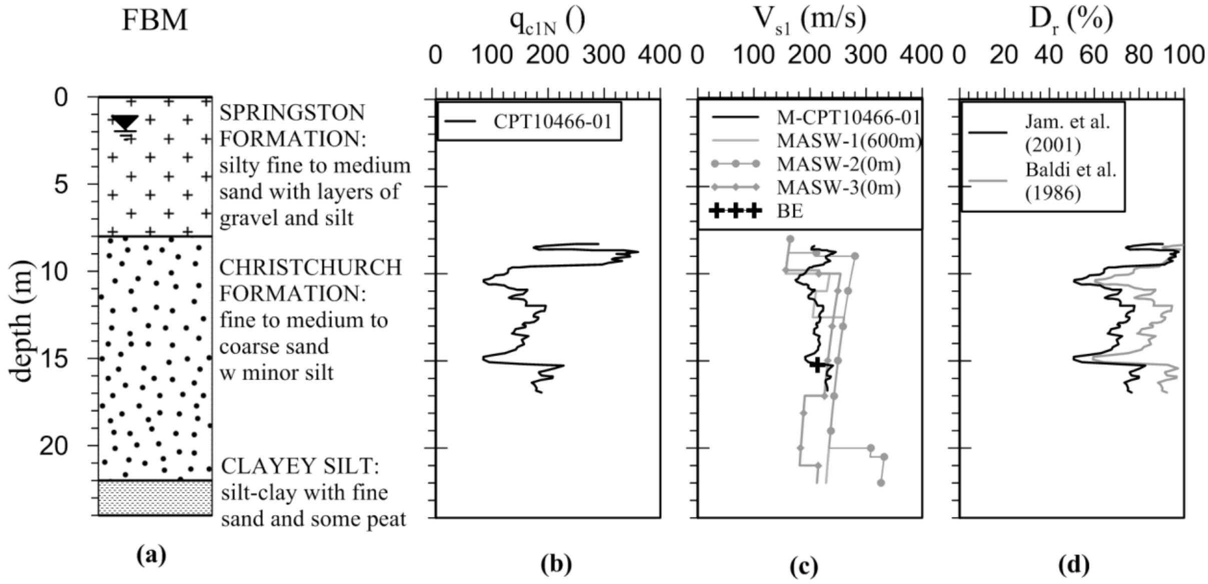

Figure B-2: FBM site (a) Summary borehole, (b) normalised CPT penetration resistance, q_{c1N}, (c) normalised V_{s1} profile (CPT correlations (M-CPT), Multi-channel Analysis of Surface Waves (MASW), bender element (BE)), (d) inferred relative density (after Taylor, 2015; NZGD, 2016)

Table B-1: Available field tests, soil samples and element testing at the K1 site

Available field tests	**Available samples**	**Available element testing**
Borehole logs (Taylor, 2015; NZGD, 2016)	Piston sampler undisturbed Gel-Push (GP) samples between depths of 2 and 6 m (fluvial sands of the Springston Formation) (Taylor, 2015)	Isotropically consolidated drained (CID) and undrained (CIU) monotonic triaxial compression tests on GP & MT samples of the Springston & Christchurch Formation (Taylor, 2015)
CPT's and CPTu's (Taylor, 2015; NZGD, 2016)	Piston sampler undisturbed Gel-Push (GP) samples between depths of 11 and 13 m (marine sands of the Christchurch Formation) (Taylor, 2015)	Isotropically consolidated undrained cyclic triaxial tests on GP & MT samples of the Springston & Christchurch Formation (Taylor, 2015)
Downhole V_s (Taylor, 2015)	Moist-tamped (MT) reconstituted specimens (Taylor, 2015)	Bender element (BE) tests on GP samples of the Springston & Christchurch Formation (Taylor, 2015)

Table B-2: Available field tests, soil samples and element testing at the FBM site

Available field tests	Available samples	Available element testing*
Borehole logs (NZGD, 2016)	Moist-tamped (MT) reconstituted specimens from a depth of about 5 to 15 m (Springston & Christchurch Formation) (Rees, 2010; Arefi, 2014; Taylor, 2015)	Isotropically consolidated drained (CID) monotonic triaxial compression tests on MT sand specimens of different FC (Taylor, 2015)
CPTs (NZGD, 2016)		Isotropically consolidated undrained cyclic triaxial tests on MT sand specimens of different FC (Taylor, 2015)
Multi-channel Analysis of Surface Waves (MASW) measurements (NZGD, 2016)		Bender element tests on MT sand specimens of different FC (Arefi, 2014)

*Triaxial testing by Arefi (2014) and Rees (2010) on FBM MT sand samples were also performed, however, detailed data were not available in the associated references and, hence, these were not used in the calibration.

Table B-3: Representative (average) gradation and index properties of the sample types used in the calibration of the BSPM (after Taylor, 2015; Rees, 2010)

Representative/average	K1 FC0-5%	K1 FC15-20%	FBM FC0%
Fines content	0% to 5%	15% to 20%	0%
D_{10}	0.115	0.060	0.089
D_{50}	0.245	0.125	0.168
C_u	2.650	2.430	2.000
$e_{0,max}$	1.010	1.105	0.907
$e_{0,min}$	0.605	0.600	0.628

Acknowledgements

The first author would like to gratefully acknowledge the financial support by the Engineering and Physical Sciences Research Council (EPSRC, 1386368). Dr. Liam Wotherspoon is also acknowledged for providing data on the local stratigraphy in Christchurch.

References

Aoi, S., Kunugi, T. & Fujiwara, H. (2008) Trampoline effect in extreme ground motion. *Science (New York, N.Y.)*. 322 (5902), 727–730.

Abrahamson, N.A. & Silva, W.J. (1997) Empirical response spectral attenuation relations for shallow crustal earthquakes. *Seismological research letters*. 68 (1), 94–127.

Amorosi, A., Rollo, F. & Boldini, D. (2018) A modified bounding surface plasticity model for sand. In: *Numerical Methods in Geotechnical Engineering IX, Volume 1: Proceedings of the 9th European Conference on Numerical Methods in Geotechnical Engineering (NUMGE 2018), June 25-27, 2018, Porto, Portugal*. 2018 p. 213.

Andrianopoulos, K.I., Papadimitriou, A.G. & Bouckovalas, G.D. (2010) Bounding surface plasticity model for the seismic liquefaction analysis of geostructures. *Soil Dynamics and Earthquake Engineering*. 30 (10), 895–911.

Arefi, M.J. (2014) *Dynamic characteristics and evaluation of ground response for sands with non-plastic fines*. PhD thesis, University of Canterbury, Christchurch, New Zealand.

Arulanandan, K. & Scott, R.F. (1993) Verification of numerical procedures for the analysis of soil liquefaction problems. *Proceedings of the International Conference on the Verification of Numerical Procedures for the Analysis of Soil Liquefaction Problems, Davis, California*. 1993 Rotterdam, the Netherlands, Balkema.

Arulanandan, K. & Sybico, J. (1993) Post-liquefaction settlement of sands. In: *Proceedings of the Wroth Memorial Symposium*. 1993 St. Catherine's College, Oxford, Thomas Telford, London. pp. 94–110.

Balakrishnan, A. (2000) *Liquefaction remediation at a bridge site*. PhD thesis, Davis University of California.

Baldi, G., Bellotti, R., Ghionna, N., Jamiolkowski, M., et al. (1986) Interpretation of CPT's and CPTU's, 2nd part, drained penetration of sands. *4th International Geotechnical Seminar*. 1986 Singapore.

Bardet, J.P., Ichii, K. & Lin, C.H. (2000) *EERA: a computer program for equivalent-linear earthquake site response analyses of layered soil deposits*. University of Southern California, Department of Civil Engineering.

Bathe, K.J. (1996) *Finite element procedures*. Englewood Cliffs, New Jersey, Prentice Hall.

Beavan, J., Fielding, E., Motagh, M., Samsonov, S., et al. (2011) Fault location and slip distribution of the 22 February 2011 Mw 6.2 Christchurch, New Zealand, earthquake from geodetic data. *Seismological Research Letters*. 82 (6), 789–799.

Been, K. & Jefferies, M.G. (1985) A state parameter for sands. *Géotechnique*. 35 (2), 99–112.

Berrill, J.B., Davis, R.O. & McCahon, I.F. (1993) Christchurch seismic hazard pilot study. *Bulletin of the New Zealand National Society for Earthquake Engineering*. 26 (1), 14–27.

Biot, M.A. (1941) General Theory of Three-Dimensional Consolidation. *Journal of Applied Physics*. 12 (2), 155.

Biot, M.A. (1956) Theory of propagation of elastic waves in a fluid-saturated porous solid. *The Journal of the Acoustical Society of America*. 28 (2), 168–191.

Boulanger, R.W. & Ziotopoulou, K. (2013) Formulation of a sand plasticity plane-strain model for earthquake engineering applications. *Soil Dynamics and Earthquake Engineering*. 53, 254–267.

Bozorgnia, Y. & Campbell, K.W. (2016) Vertical Ground Motion Model for PGA, PGV, and Linear Response Spectra Using the NGA-West2 Database. *Earthquake Spectra*. 32 (2), 979–1004.

Bradley, B.A. (2010) *NZ-specific pseudo-spectral acceleration ground motion prediction equations based on foreign models*. Research Report 2010-03, University of Canterbury [Online]. p.324. Available from: http://hdl.handle.net/10092/5126.

Bradley, B.A. (2013) A New Zealand-specific pseudospectral acceleration ground-motion prediction equation for active shallow crustal earthquakes based on foreign models. *Bulletin of the Seismological Society of America*. 103 (3), 1801–1822.

Bradley, B.A. & Cubrinovski, M. (2011) Near-source strong ground motions observed in the 22 February 2011 Christchurch earthquake. *Seismological Research Letters*. [Online] 82 (6), 853–865. Available from: doi:10.1785/gssrl.82.6.853.

Brown, L.J., Beetham, R.D., Paterson, B.R. & Weeber, J.H. (1995) Geology of Christchurch, New Zealand. *Environmental & Engineering Geoscience*. 1 (4), 427–488.

Campbell, K.W. & Bozorgnia, Y. (2003) Updated near-source ground-motion (attenuation) relations for the horizontal and vertical components of peak ground acceleration and acceleration response spectra. *Bulletin of the Seismological Society of America*. 93 (1), 314–331.

Carman, P. (1956) *Flow of gases through porous media*. London: Butterworth.

Chung, J. & Hulbert, G.M. (1993) A time integration algorithm for structural dynamics with improved numerical dissipation: the generalised-α method. *Journal of Applied Mechanics*. 60 (2), 371–375.

Coelho, P.A.L.F. (2007) *In situ densification as a liquefaction resistance measure for bridge foundations*. PhD thesis, University of Cambridge.

Dafalias, Y.F. & Manzari, M.T. (2004) Simple Plasticity Sand Model Accounting for Fabric Change Effects. *Journal of Engineering Mechanics*. 130 (6), 622–634.

Dafalias, Y.F. & Taiebat, M. (2016) SANISAND-Z: zero elastic range sand plasticity model. *Géotechnique*. 66 (12), 999–1013.

Darendeli, M.B. (2001) *Development of a new family of normalised modulus reduction and material damping curves*. PhD thesis. University of Texas, Austin.

Elder, D.M., McCahon, I.F. & Yetton, M.D. (1991) *The earthquake hazard in Christchurch: a detailed evaluation*. Soils and Foundations Ltd.

Frydman, S., Hendon, D., Horn, H., Baker, R., et al. (1980) Liquefaction study of cemented sand. *Journal of Geotechnical and Geoenvironmental Engineering*. 106 (GT3), 275–297.

Gao, H., Hu, B. & Chang, D. (1983) Some geological considerations for the damage during the Tangshan earthquake. *North China Earthquake Sciences*. 164–72.

Garini, E., Panagoulias, S., Tasiopoulou, P. & Gazetas, G. (2013) Canterbury earthquakes: the Resthaven records and soil amplification response. *ICEGE, from case history to practice; In honour of Prof. Kenji Ishihara*. 2013 Istanbul, Turkey.

GNS Science (2012) *Consultancy Report 2012/218 - Appendix 5: Geological information relevant to the liquefaction hazard assessment and liquefaction susceptibility zoning*. pp.63–95.

Green, R.A., Cubrinovski, M., Cox, B., Wood, C., et al. (2014) Select liquefaction case histories from the 2010-2011 Canterbury earthquake sequence. *Earthquake Spectra*. 30 (1), 131–153.

Han, B. (2014) *Hydro-mechanical coupling in numerical analysis of geotechnical structures under multi-directional seismic loading*. PhD thesis, Department of Civil & Environmental Engineering, Imperial College London, London.

Han, B., Zdravkovic, L. & Kontoe, S. (2015a) Stability investigation of the Generalised-α time integration method for dynamic coupled consolidation analysis. *Computers and Geotechnics*. 6483–95.

Han, B., Zdravković, L. & Kontoe, S. (2018) Analytical and numerical investigation of site response due to vertical ground motion. *Géotechnique*. 68 (6), 467–480.

Hazen, A. (1892) *Some physical properties of sands and gravels, with special reference to their use in filtration*, volume 34, pp. 539-556.

Idriss, I.M. & Boulanger, R.W. (2008) *Soil liquefaction during earthquakes*. Oakland,California, USA, Earthquake Engineering Research Institute.

Ishihara, K. (1985) Stability of natural deposits during earthquakes. In: *11th International Conference on Soil Mechanics and Foundation Engineering, San Francisco, Vol. I*. 1985 AA Balkema. pp. 321–376.

Ishihara, K. (1996) *Soil behaviour in earthquake geotechnics*. Oxford Engineering Series. Oxford, Oxford University Press.

Jaky, J. (1944) The coefficient of earth pressure at rest. *Journal for Society of Hungarian Architects and Engineers*. 7, 355–358.

Jamiolkowski, M., Lo Presti, D.C.F. & Manassero, M. (2003) Evaluation of relative density and shear strength of sands from CPT and DMT. *Soil Behavior and Soft Ground Construction*. 7 (119), 201–238.

Kokusho, T., Yoshida, Y., Nishi, K. & Esashi, Y. (1983) Evaluation of seismic stability of dense sand layer (part 1) - dynamic strength characteristics of dense sand. Electric Power Central Research Institute, *Report* 383025, Japan.

Kontoe, S. (2006) *Development of time integration schemes and advanced boundary conditions for dynamic geotechnical analysis*. PhD thesis, Department of Civil & Environmental Engineering, Imperial College London, London.

Kontoe, S., Zdravković, L. & Potts, D.M. (2008) An assessment of time integration schemes for dynamic geotechnical problems. *Computers and Geotechnics*. 35 (2), 253–264.

Kozeny, J. (1927) Uber kapillare Leitung des Wassers im Boden. *Akad. der Wissenschaften*. 136 (2a).

Kramer, S.L. (1996) *Geotechnical Earthquake Engineering*. Englewood Cliffs, New Jersey, Prentice Hall.

Kulhawy, L.H. & Mayne, P.H. (1990) *Manual on etsimating soil properties for foundation design*. Available from: http://www.geoplanning.it/test/wp-content/uploads/2012/02/manual-on-estimating-soil-properties-for-foundation-design.pdf.

Lee, R.L., Franklin, M.J. & Bradley, B.A. (2013) Characteristics of vertical ground motions in the Canterbury earthquakes. *New Zealand Society for Earthquake Engineering Annual Conference (NZSEE2013)*. 2013 Wellington, University of Canterbury.

López-Querol, S. & Blázquez, R. (2006) Liquefaction and cyclic mobility model for saturated granular media. *International Journal for Numerical and Analytical Methods in Geomechanics*. 30 (5), 413–439.

Loukidis, D. & Salgado, R. (2009) Modeling sand response using two-surface plasticity. *Computers and Geotechnics*. 36 (1-2), 166–186.

Lunne, T., Christoffersen, H.P. & others (1983) Interpretation of cone penetrometer data for offshore sands. *Offshore Technology Conference*. 1983.

Lunne, T., Robertson, P.K. & Powell, J.J.M. (1997) *Cone penetration testing in geotechnical practice*. Taylor & Francis.

Manzari, M.T. & Arulanandan, K. (1993) Numerical predictions for model No 1. In: K. Arulanandan & R.F. Scott (eds.). *Verification of Numerical Procedures for the Analysis of Soil Liquefaction Problems, Proceedings of the International Conference, Davis, California*. 1993 Rotterdam, the Netherlands, Balkema.

Manzari, M.T. & Dafalias, Y.F. (1997) A critical state two-surface plasticity model for sands. *Géotechnique*. 47 (2), 255–272.

Markham, C.S., Bray, J.D., Macedo, J. & Luque, R. (2016) Evaluating nonlinear effective stress site response analyses using records from the Canterbury earthquake sequence. *Soil Dynamics and Earthquake Engineering*. 82, 84–98.

Muraleetharan, K.K. (1993) Numerical predictions for model No. 4a. In: K. Arulanandan & R.F. Scott (eds.). *Verification of Numerical Procedures for the Analysis of Soil Liquefaction*

Problems, Proceedings of the International Conference, Davis, California. 1993 Rotterdam, the Netherlands, Balkema. pp. 641–650.

McGann, C.R., Bradley, B.A., Cubrinovski, M., Taylor, M.L., et al. (2014a) *Development and evaluation of CPT-Vs correlation for Canterbury, New Zealand soils of the shallow Christchurch and Springston formations*. Report 2014-01, University of Canterbury.

Nishio, N., Tamaoki, K. & Machida, Y. (1985) Dynamic deformation characteristics of crushed gravel by means of large-size triaxial test apparatus. *Proceedings of the 20th Annual Convention, Japanese Society of Soil Mechanics and Foundation Engineering*. 1985 pp. 603–604.

NZGD (2016) *New Zealand Geotechnical Database - MBIE & EQC*. 2016. Available from: www.nzgd.org.nz [Accessed: 30 September 2016].

Papadimitriou, A.G. & Bouckovalas, G.D. (2002) Plasticity model for sand under small and large cyclic strains: A multiaxial formulation. *Soil Dynamics and Earthquake Engineering*. 22 (3), 191–204.

Potts, D.M. & Zdravković, L. (1999) *Finite element analysis in geotechnical engineering: theory*. London, Thomas Telford.

Prevost, J. (1978) Plasticity theory for soil stress-strain behavior. *Journal of the Engineering Mechanics Division*. 104 (5), 1177–1194.

Rees, S. (2010) *Effects of fines on undrained behaviour of sands*. PhD thesis, University of Canterbury, Christchurch, New Zealand. Available from: doi:10.1061/40975(318)91.

Robertson, P.K. (2012) Interpretation of in-situ tests-some insights. *James K. Mitchell Lecture, Proc. 4th Int. Conf. on Geotechnical and Geophysical Site Characterization-ISC'4*. 2012 Porto de Galinhas, Pernambuco, Brazil. pp. 1–22.

Robertson, P.K. & Cabal, K.L. (2012) *Guide to cone penetration testing*. [Online]. p.145. Available from: http://www.novotechsoftware.com/downloads/PDF/en/Ref/CPT-Guide-5ed-Nov2012.pdf

Robertson, P.K. & Wride, C.E. (1998) Evaluating cyclic liquefaction potential using the cone penetration test. *Canadian Geotechnical Journal*. 35 (3), 442–459.

Rollins, K.M., Evans, M.D., Diehl, N.B. & III, W.D.D. (1998) Shear modulus and damping relationships for gravels. *Journal of Geotechnical and Geoenvironmental Engineering*. 124 (5), 396–405.

Seed, R.B. & Harder, L.F. (1990) SPT-based analysis of cyclic pore pressure generation and undrained residual strength. Proceedings of the *H. Bolton Seed Memorial Symposium*. 1990 pp. Vol. 2. 351–376.

Shahir, H., Mohammadi-Haji, B. & Ghassemi, A. (2014) Employing a variable permeability model in numerical simulation of saturated sand behavior under earthquake loading. *Computers and Geotechnics*. 55, 211–223.

Smyrou, E., Tasiopoulou, P., Bal, I.E. & Gazetas, G. (2011) Ground motions versus geotechnical and structural damage in the February 2011 Christchurch earthquake. *Seismological Research Letters*. 82 (6), 882–892.

Su, D., Li, X.-S. & Xing, F. (2009) Estimation of the apparent permeability in the dynamic centrifuge tests. *Geotechnical Testing Journal*. 32 (1), 1–9.

Taborda, D.M.G. (2011) *Development of constitutive models for application in soil dynamics*. PhD thesis, Department of Civil & Environmental Engineering, Imperial College London.

Taborda, D.M.G., Potts, D.M. & Zdravković, L. (2016) On the assessment of energy dissipated through hysteresis in finite element analysis. *Computers and Geotechnics*. 71, 180–194.

Taborda, D.M.G. & Zdravkovic, L. (2012) Application of a Hill-Climbing technique to the formulation of a new cyclic nonlinear elastic constitutive model. *Computers and Geotechnics*. 43, 80–91.

Taborda, D.M.G., Zdravković, L., Kontoe, S. & Potts, D.M. (2014) Computational study on the modification of a bounding surface plasticity model for sands. *Computers and Geotechnics*. 59, 145–160.

Taiebat, M., Shahir, H. & Pak, A. (2007) Study of pore pressure variation during liquefaction using two constitutive models for sand. *Soil Dynamics and Earthquake Engineering*. 27 (1), 60–72.

Tasiopoulou, P., Smyrou, E., Bal, I.E., Gazetas, G., et al. (2011) Geotechnical and structural field observations from Christchurch, February 2011 earthquake, in New Zealand. Research report, *National Technical University of Athens (NTUA), Athens, Greece*.

Taylor, M.L. (2015) *The geotechnical characterisation of Christchurch sands for advanced soil modelling*. PhD thesis, University of Canterbury.

Tsaparli, V. (2017) *Numerical modelling of earthquake-induced liquefaction under irregular and multi-directional loading*. PhD thesis, Department of Civil & Environmental Engineering, Imperial College London, London.

Tsaparli, V., Kontoe, S., Taborda, D.M.G. & Potts, D.M. (2016) Vertical ground motion and its effects on liquefaction resistance of fully saturated sand deposits. *Proceedings of the Royal Society A: Mathematical, Physical and Engineering Sciences*. 472 (2192).

Tsaparli, V., Kontoe, S., Taborda, D.M.G. & Potts, D.M. (2017a) An energy-based interpretation of sand liquefaction due to vertical ground motion. *Computers and Geotechnics*. 90, 1–13.

Tsaparli, V., Kontoe, S., Taborda, D.M.G. & Potts, D.M. (2017b) The importance of accurate time-integration in the numerical modelling of P-wave propagation. *Computers and Geotechnics*. 86, 203–208.

Tsaparli, V., Kontoe, S., Taborda, D.M.G. & Potts, D.M. (2018) Liquefaction triggering due to compressional waves: validation through field records. In: K. Pitilakis (ed.). *16th European Conference on Earthquake Engineering*. 2018 Thessaloniki, Greece.

Vaid, Y.P. & Thomas, J. (1994) Post-liquefaction behaviour of sand. *Proceedings of the 13th International Conference on Soil Mechanics and Foundation Engineering*. 1994 New Delhi. pp. 1303–1310.

Van Ballegooy, S., Cox, S.C., Thurlow, C., Rutter, H.K., et al. (2014) Median water table elevation in Christchurch and surrounding area after the 4 September 2010 Darfield Earthquake: Version 2. *GNS Science Report*. 18.

Wood, C.M., Cox, B.R., Wotherspoon, L.M. & Green, R.A. (2011) Dynamic site characterization of Christchurch strong motion stations. *Bulletin of the New Zealand Society for Earthquake Engineering*. 44 (4), 195–204.

Wotherspoon, L.M., Orense, R., Bradley, B.A., Cox, B.R., et al. (2015) *Geotechnical characterization of Christchurch strong motion stations V3*. Earthquake Commision Report (Project No. 12/629), the University of Auckland. Available from: http://library.canterbury.ac.nz/ir/rights.shtml.

Yamada, M., Mori, J. & Heaton, T. (2009) The slapdown phase in high-acceleration records of large earthquakes. *Seismological Research Letters*. 80 (4), 559–564.

Yoshida, Y., Ikemi, M. & Kokusho, T. (1988) Empirical formulas of SPT blow-counts for gravelly soils. In: J De Ruiter (ed.). *Proc 1st International Symposium on Penetration Testing, ISOPT-1*. 1988 20-24 March 1988, Orlando, USA, Rotterdam, AA Balkema. pp. 381–387.

Zienkiewicz, O.C., Bicanic, N. & Shen, F.Q. (1988) Earthquake input definition and the transmitting boundary conditions. In: I. St Doltsinis (ed.). *Advances in Computational Nonlinear Mechanics*. Vienna, Austria, pp. 109–138.

Zienkiewicz, O.C., Chang, C.T. & Bettess, P. (1980) Drained, undrained, consolidating and dynamic behaviour assumptions in soils. *Géotechnique*. 30 (4), 385–395.

Figure captions

Figure 1: SMS PRPC (a) Summary borehole, (b) normalised CPT penetration resistance, qc1N, (c) soil behaviour type index, Ic, (Robertson & Wride, 1998) (d) overburden-stress corrected shear wave velocity, Vs1, profiles (NZGD, 2016; Wotherspoon *et al.*, 2015)

Figure 2: Relative density profile with depth for the sand layers at PRPC as obtained through CPT-Dr correlations

Figure 3: Back-calculation of Vs for the K1 GP samples for (a) a B of 420 based on bender element tests and (b) a B of 500 to better fit the downhole (DH) measurements (Taylor, 2015) and CPT_Vs (McGann *et al.*, 2014, M-CPT) correlations

Figure 4: Comparison of the initial states of the GP samples with FC 0-20%, as obtained for the calibrated CLS of this study, with a CPT-ψ correlation for the K1 site based on Robertson (2012)

Figure 5: Computed Kσ trend of Christchurch sand for cyclic simple shear conditions for a Dr of 70% and comparison with available laboratory and field data (Vaid & Thomas, 1994; Seed & Harder, 1990; Kokusho *et al.*, 1983; Frydman *et al.*, 1980; Idriss & Boulanger, 2008)

Figure 6: Darendeli (2001) normalised stiffness degradation and damping variation curves and ICG3S calibrated curves for the sandy/clayey silt layers at (a) 0-3 m, (b) 20-22 m and (c) 26.5-28 m depth

Figure 7: (a) Input motion for analysis LS3 and (b) comparison of computed ground surface acceleration time-history with the recorded East-West (W) ground surface motion at PRPC

Figure 8: (a) Input motion for analysis RN1 and (b) comparison of computed ground surface acceleration time-history with the recorded East-West (W) ground surface motion at PRPC

Figure 9: (a) Input motion for analysis LV1 and (b) comparison of computed ground surface acceleration time-history with the recorded vertical (UP) ground surface motion at PRPC

Figure 10: (a) Initial and final (end of dynamic motion) mean effective stress profile and (b) CSR time-history at 13 m depth in the sand layer for analysis LV1

Figure 11: (a) Input motion for analysis RV3 and (b) comparison of computed ground surface acceleration time-history with the recorded vertical (UP) ground surface motion at PRPC

Figure 12: Comparison of computed ground surface acceleration time-history for analysis LV1_GR with the recorded vertical (UP) ground surface motion at PRPC

Figure 13: Modelled variation of permeability with excess pore pressure ratio

Figure 14: Profiles of (a) maximum and (b) final values of r_u within the sand layers during the strong motion for analysis LS3 with variable permeability (LS3_Vk). Results of analyses LS3_k10-3 (with constant higher permeability of 10-3 m/s) and original LS3 (with constant permeability of 10-4 m/s) are also shown for comparison purposes

Figure 15: Predicted (a) co-seismic and (b) total post-liquefaction settlements at 0 and 3.25 m depth for analyses LS3 with variable permeability (LS3_Vk) and original analysis LS3 with constant permeability

Figure 16: Proposed boundaries for the prediction of ground surface manifestation of liquefaction (adapted from Figure 88, Ishihara (1985))

Figure A-1: BSPM performance in (a) undrained and (b) drained monotonic triaxial conditions

Figure A-2: BSPM performance in cyclic triaxial conditions (B_{CRR} is the slope of a power law fit to the cyclic strength data)

Figure A-3: Stiffness degradation and damping variation curves reproduced by the BSPM for initial conditions corresponding to the middle of the thick Christchurch sand layer at PRPC (i.e. 11.5 m depth) and to the field relative density, together with the corresponding curves based on Darendeli (2001).

Figure B-1: K1 site (a) Summary borehole, (b) normalised CPT penetration resistance, q_{c1N}, (c) soil behaviour type index, I_c, (d) V_{s1} profile through CPT correlations (M-CPT) and downhole (DH) measurements (after Taylor, 2015; NZGD, 2016)

Figure B-2: FBM site (a) Summary borehole, (b) normalised CPT penetration resistance, q_{c1N}, (c) normalised V_{s1} profile (CPT correlations (M-CPT), Multi-channel Analysis of Surface Waves (MASW), bender element (BE)), (d) inferred relative density (after Taylor, 2015; NZGD, 2016)

10 Table captions

Table 1: Properties of Christchurch sand with FC 0-20%

Table 2: Properties of clayey silt layers

Table 3: GMPE predictions of the largest outcrop horizontal PGA at SMS PRPC and summary of horizontal component FE analyses

Table 4: GMPE predictions of the outcrop vertical PGA at SMS PRPC and summary of vertical component FE analyses

Table 5: Properties of Riccarton gravel

Table A-1: Modified formulation of the two-surface BSPM (Tsaparli, 2017)

Table A-2: BSPM model parameters for Christchurch sand FC 0-20%

Table A-3: ICG3S model parameters for the clayey silt layers

Table A-4: ICG3S model parameters for the Riccarton gravel layer

Table B-1: Available field tests, soil samples and element testing at the K1 site

Table B-2: Available field tests, soil samples and element testing at the FBM site

Table B-3: Representative (average) gradation and index properties of the sample types used in the calibration of the BSPM (after Taylor, 2015; Rees, 2010)